

Astrocytes and oligodendrocytes undergo subtype-specific transcriptional changes in Alzheimer's disease

Highlights

- Astrocytes and oligodendrocytes have altered and heterogeneous transcriptomes in AD
- Dataset integration improves glia clustering and suggests putative altered function
- “Reactive” substates of glia are likely spatially restricted
- Astrocyte inflammation responses mimic some AD-associated gene expression changes

Authors

Jessica S. Sadick, Michael R. O’Dea,
Philip Hasel, Taitea Dykstra,
Arline Faustin, Shane A. Liddelow

Correspondence

shane.liddelow@nyulangone.org

In brief

Transcriptomic and functional changes in glia are hallmarks of Alzheimer’s disease. In this issue of *Neuron*, Sadick, O’Dea, et al. define transcriptomic differences in astrocytes and oligodendrocytes in Alzheimer’s disease at the single-nuclei level. They also localize human Alzheimer’s-associated transcription profiles to strategic location in the inflamed mouse brain.

NeuroResource

Astrocytes and oligodendrocytes undergo subtype-specific transcriptional changes in Alzheimer's disease

Jessica S. Sadick,^{1,7,8} Michael R. O'Dea,^{1,7} Philip Hasel,¹ Taitea Dykstra,^{1,9,10} Arline Faustin,^{2,3} and Shane A. Liddelow^{1,4,5,6,11,*}

¹Neuroscience Institute, NYU Grossman School of Medicine, New York, NY 10016, USA

²Center for Cognitive Neurology, NYU Grossman School of Medicine, New York, NY 10016, USA

³Department of Pathology, NYU Langone Health, New York, NY 10016, USA

⁴Department of Neuroscience and Physiology, NYU Grossman School of Medicine, New York, NY 10016, USA

⁵Department of Ophthalmology, NYU Grossman School of Medicine, New York, NY 10016, USA

⁶Parekh Center for Interdisciplinary Neurology, NYU Grossman School of Medicine, New York, NY 10016, USA

⁷These authors contributed equally

⁸Present address: Neurology Discovery, Valo Health, Boston, MA 02116, USA

⁹Present address: Center for Brain Immunology and Glia, School of Medicine, Washington University in St. Louis, St. Louis, MO 63110, USA

¹⁰Present address: Department of Pathology and Immunology, School of Medicine, Washington University in St. Louis, St. Louis, MO 63110, USA

¹¹Lead contact

*Correspondence: shane.liddelow@nyulangone.org

<https://doi.org/10.1016/j.neuron.2022.03.008>

SUMMARY

Resolving glial contributions to Alzheimer's disease (AD) is necessary because changes in neuronal function, such as reduced synaptic density, altered electrophysiological properties, and degeneration, are not entirely cell autonomous. To improve understanding of transcriptomic heterogeneity in glia during AD, we used single-nuclei RNA sequencing (snRNA-seq) to characterize astrocytes and oligodendrocytes from apolipoprotein (APOE) ε2/3 human AD and age- and genotype-matched non-symptomatic (NS) brains. We enriched astrocytes before sequencing and characterized pathology from the same location as the sequenced material. We characterized baseline heterogeneity in both astrocytes and oligodendrocytes and identified global and subtype-specific transcriptomic changes between AD and NS astrocytes and oligodendrocytes. We also took advantage of recent human and mouse spatial transcriptomics resources to localize heterogeneous astrocyte subtypes to specific regions in the healthy and inflamed brain. Finally, we integrated our data with published AD snRNA-seq datasets, highlighting the power of combining datasets to resolve previously unidentifiable astrocyte subpopulations.

INTRODUCTION

Alzheimer's disease (AD) is the most common age-related neurodegenerative disorder in the world and accounts for about 70% of the 50 million people with dementia worldwide, with an estimated 10 million new cases every year, or close to 20 new cases every minute (Alzheimer's Association, 2021). With an aging population, greater understanding of AD pathogenesis is imperative for the development of effective therapies. Defined by progressive memory and cognitive loss, AD is a disease of proteopathic stress associated with abnormal beta-amyloid (Aβ) and tau aggregation, and neuron death (De Strooper and Karran, 2016; Ginsberg et al., 2006; Mattsson et al., 2016; Yue and Jing, 2015). More recently, research highlights non-neuronal central nervous system (CNS) cells, namely glia, as active contributors to AD pathophysiology. Increasing evidence supports a pathological role of "reactive" astrocytes in acute and chronic

diseases, such as AD (Carter et al., 2012; Owen et al., 2009; Sadick and Liddelow, 2019; Schipper et al., 2006). This includes changes in normal physiological functions, such as synapse maintenance (Hong et al., 2016), blood-brain barrier (BBB) integrity (de la Torre, 2004; Farkas and Luiten, 2001; Viswanathan and Greenberg, 2011), metabolism (González-Reyes et al., 2017), and structural support (Mohamed et al., 2016; Teakpong et al., 2003; Wu et al., 2015). Many studies implicate reactive astrocytes induced by immune cell dysfunction and inflammatory responses to pathogenic proteins (Aβ and tau) and dying cells (Hasel et al., 2021; Liddelow et al., 2017; Shi et al., 2017; Zamanian et al., 2012). Oligodendrocytes are also of interest in AD pathology given their role in myelin production and axon support (Fünfschilling et al., 2012; Saab et al., 2016). White matter (WM) abnormalities (e.g., lesions, decreased volume, and microstructural deterioration) and demyelination are well documented in AD (Lee et al., 2016; Radanovic et al., 2013). Beyond these

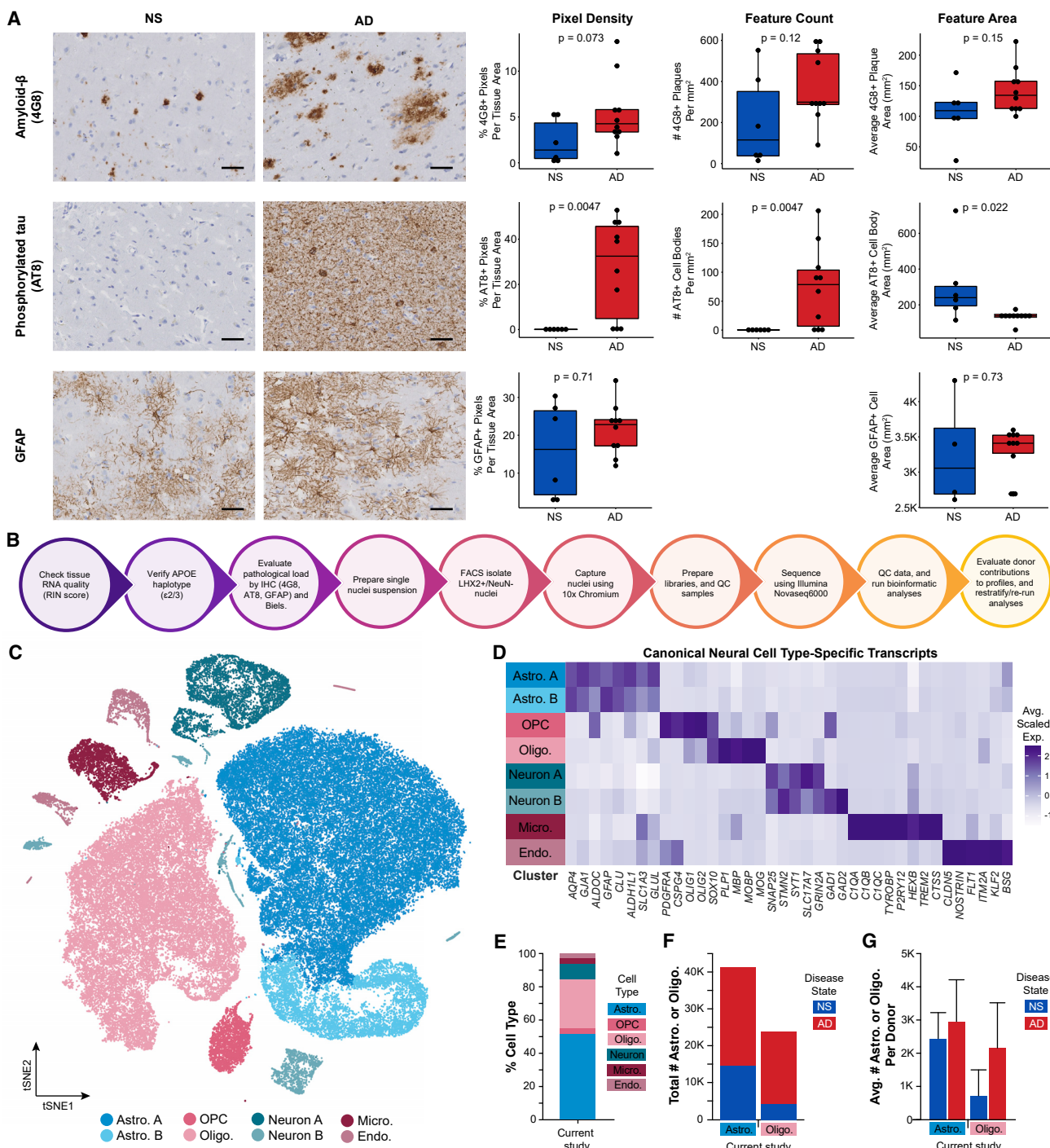


Figure 1. Defining a well-controlled patient cohort is key for defining AD-associated gene expression profiles

(A) Representative micrographs and corresponding quantification in NS and AD donors of immunohistochemistry for amyloid- β plaques (4G8), phosphorylated tau (AT8), and GFAP. Scale bars represent 50 μ m. Raw quantification values are displayed as well as mean \pm SD.

(B) Workflow for donor quality control and astrocyte enrichment strategy.

(C) tSNE plot of total nuclei (N = 80,247) showing clusters of Astrocytes (blue), Oligodendrocytes (pink), Neurons (teal), Microglia (dark purple), and Endothelial cells (light purple).

(D) Corresponding average scaled expression heatmap of cell-type-specific transcripts by cluster.

(E) Cell-type proportions of total nuclei captured.

(F) Total numbers of astrocytes and oligodendrocytes captured split by disease state.

(G) Avg. # Astro or Oligo. Per Donor.

(legend continued on next page)

broad physiological changes, many questions remain, such as how subtypes of astrocytes and oligodendrocytes are altered in AD.

Single-nuclei RNA sequencing (snRNA-seq) has been used to assess cellular heterogeneity at the transcriptomic level in human AD postmortem brains (Del-Aguila et al., 2019; Gerrits et al., 2021; Grubman et al., 2019; Lau et al., 2020; Leng et al., 2021; Mathys et al., 2019; Zhou et al., 2020). In most studies, however, astrocytes are underrepresented, making up only ~3%–18% of nuclei. Therefore, we posited that these studies may not provide large enough samples to confidently define biologically important, but lowly abundant, astrocyte subpopulations—a hypothesis supported by the fact that similar subpopulations are not identified across published datasets. In contrast, oligodendrocytes are well represented in snRNA-seq studies, with some agreement in identified subpopulations. In addition, given the important spatially confined responses of astrocytes to AD pathology (e.g., surrounding amyloid plaques or near-degenerated brain regions), no studies have combined pathological characterization with sequencing efforts on the same tissue samples. Several studies have provided pathological analysis of contralateral or adjacent brain regions, but these may be far removed from local pathology-induced microenvironments (Gerrits et al., 2021; Leng et al., 2021; Mathys et al., 2019). A lack of concordance may also be reflective of variability with respect to pathological load and/or underlying genetic variance across donors.

Here, we present a snRNA-seq dataset characterizing astrocytes and oligodendrocytes isolated from human postmortem prefrontal cortex samples from AD and age-matched non-symptomatic (NS) patients. All individuals were genotyped and controlled for apolipoprotein (APOE) genotype ε2/3. We chose this patient population as it is underrepresented in other sequencing studies and individuals present with AD dementia onset at later ages (onset ~80 years [Reiman et al., 2020]), making age matching between NS and AD patients more similar. In addition, APOEε2/3 individuals have a low odd-risk ratio of contracting AD compared with individuals that carry an APOEε4 allele (Goldberg et al., 2020; Reiman et al., 2020).

In order to improve astrocyte capture for snRNA-seq, we enriched astrocytes by sorting nuclei based on LIM Homeobox 2 (LHX2)-positive/NeuN-negative staining followed by 10X-Genomics-based snRNA-seq. This method enriches astrocytes while maintaining capture rates of oligodendrocytes and depleting neurons. We characterized the pathology of donor tissue from the same location that nuclei were isolated for sequencing. We identified global and subtype-specific transcriptomic changes between AD and NS astrocytes and oligodendrocytes. Additionally, we localized heterogeneous astrocyte subtypes to specific cortical regions in the healthy and inflamed brain using published human and mouse spatial transcriptomics datasets. Lastly, we integrated our data with published AD snRNA-seq datasets and resolved unique astrocyte subpopulations present across

datasets. Overall, we provide a paired sequencing and pathology assessment resource that can be used to further explore the breadth of astrocyte and oligodendrocyte transcriptomic changes in AD.

RESULTS

Defining a well-controlled patient cohort is key for defining AD-associated gene expression profiles

We first decided to reanalyze and compare three recent studies (Grubman et al., 2019; Mathys et al., 2019; Zhou et al., 2020) and found that astrocytes made up on average $15\% \pm 8.7\%$ of total nuclei captured (2,300–23,000 per study—on average less than 400 astrocytes per donor; Figures S1A–S1C; Table S1). Given that astrocytes are one of the most abundant CNS cell types (Nedergaard et al., 2003; von Bartheld et al., 2016), this low capture rate was surprising. In contrast, other cell populations were well represented. In addition, donors varied in APOE genotype, which may confound resulting profiles of astrocytes, given they highly express APOE (Zhang et al., 2016). Therefore, we focused on APOE ε2/3 donors, a population of patients that has been understudied. Our approach enabled us to (1) conduct a highly stringent evaluation of our donor cohort and (2) optimize enrichment methods for astrocytes prior to sequencing for improved astrocyte capture rates.

We characterized our patient cohort by verifying APOE genotype (Figure S1D) and evaluating pathological load of donor tissue for Aβ (4G8), phosphorylated tau (AT8), glial fibrillary acidic protein (GFAP), and Bielschowsky's silver staining (Figure 1A; Table S2). Each stain was quantified for normalized staining density, total count of features (i.e., number of 4G8⁺ Aβ plaques or AT8⁺ cell bodies), and average cross-sectional area of each feature (Table S2). We evaluated diffuse plaques, neuritic plaques, and neurofibrillary tangle loads (Table S2). In line with clinical diagnoses, phosphorylated tau staining density and total number of AT8⁺ cell bodies were significantly higher in AD donors compared with NS donors ($p = 0.0047$). In contrast, we did not detect major differences in Aβ plaque staining density or area or GFAP⁺ staining density or area between disease conditions. Interestingly, individual AT8⁺ cell bodies were significantly larger in NS donors than in AD donors ($p = 0.022$)—likely driven by differences in the number of AT8⁺ cell bodies detected between disease conditions (AT8⁺ cell bodies counted: 141 NS versus 57,829 AD). Based on Bielschowsky's silver staining, we classified NS donors as having no or low pathology loads, whereas AD donors had moderate or severe pathology loads.

We next sought to improve astrocyte capture for snRNA-seq by enriching astrocytic nuclei prior to sequencing (Figure S2). Initially, we attempted astrocyte enrichment via SOX9 sorting (Figures S1E–S1G and S2A), given SOX9 is a transcription factor highly and uniquely expressed in astrocytes (Zhang et al., 2016). However, this strategy proved ineffective in increasing astrocyte capture yields, likely due to non-specific SOX9 antibodies

(G) Average number of astrocytes and oligodendrocytes captured per donor split by disease state: NS (blue), AD (red). Abbreviations are as follows: AD, Alzheimer's disease; Astro., astrocyte; Endo., endothelial cell; FACS, fluorescence-activated cell sorting; GFAP, glial fibrillary acidic protein; IHC, immunohistochemistry; Micro., microglia; NS, non-symptomatic; Oligo., oligodendrocyte; OPC, oligodendrocyte precursor cell; and RIN, RNA integrity number. See also Figures S1–S3.

(Table S3). Instead, we turned to a dual immunolabeling strategy pioneered by Nott and colleagues (Nott et al., 2019) by sorting samples based on LHX2⁺NeuN⁻ (Figures S1H–S1M and S2B; Table S3). Using this strategy, we enriched astrocytes, maintained oligodendrocyte numbers, and depleted neurons (Figures 1C–1G). While optimizing this process, we sorted a single donor using both sorting strategies, highlighting significant improvement in total astrocyte capture (Figures S1H–S1M). Overall, in our final donor cohort, 51.5% of nuclei captured were astrocytes, totaling 41,340 astrocytes and averaging $2,756 \pm 1,087$ astrocytes per donor (Figures 1E–1G). In addition, 29.7% of nuclei captured were oligodendrocytes, totaling 23,840 oligodendrocytes and averaging $1,589 \pm 1,342$ oligodendrocytes per donor (Figures 1E–1G).

Putative loss of critical oligodendrocyte functions in AD

We identified five unique oligodendrocyte transcriptomically defined clusters (Figures 2A and 2B) and evaluated these gene sets on their own and by gene ontology (GO)/pathway analysis (Table S4). We did not identify any singular sample variable, such as disease state, sex, RNA quality, age of donor, or post-mortem interval (PMI), that was exclusively associated with a cluster (Figures 2C and S3). Although few genes were exclusively expressed by a single cluster, several were enriched in some clusters over others. Oligodendrocyte cluster 1, for example, was enriched for transcripts involved in glial cell development (*PLP1*, *CNP*, and *CD9*) and apoptotic signaling (*SEPTIN4* and *SERINC3*). Oligodendrocyte cluster 2 was enriched for transcripts associated with cholesterol metabolism (*MSMO1*, *FDFT1*, and *LSS*). Oligodendrocyte clusters 2, 3, and 4 were enriched for transcripts involved in synapse assembly and organization. Additionally, oligodendrocyte cluster 4 expresses transcripts involved in antigen processing/presentation (*PSMB1*, *B2M*, and *HLA-A*) and innate-immunity-associated pathways, such as interleukin-1 signaling, tumor necrosis factor signaling, and NF- κ B signaling. Finally, although we did not identify any statistically significant GO terms associated with oligodendrocyte cluster 0, based on cluster-enriched differentially expressed genes (DEGs), we inferred that this cluster was associated with synapse organization and aspects of metabolism (Table S3).

We next evaluated differential gene expression between AD and NS oligodendrocytes using *edgeR* paired with *zinbwave*-generated observational weights. We identified 358 unique upregulated and 227 unique downregulated DEGs in AD oligodendrocytes (Table S4). We did not find any transcriptomic changes that were conserved/common across all oligodendrocyte subpopulations but instead found highly cluster-specific transcriptomic changes based on disease state (Figures 2D–2I).

We next classified our findings by assigning “GO descriptions”—a manual evaluation of oligodendrocyte-cluster-specific or oligodendrocyte-cluster-shared GO terms. This allowed us to summarize multiple identified GO terms associated with either upregulated or downregulated pathways, for single or multiple oligodendrocyte clusters (Figures S4 and S5; Table S4). Oligodendrocyte “GO descriptions” associated with AD fell into two broad categories: upregulation of synaptic maintenance or downregulation of synaptic maintenance. For example, cluster 1 AD oligodendrocytes upregulate GO terms associated with axonogenesis and

synapse organization (examples associated DEGs include *LRP4*, *TIAM1*, and *CDH2*). Decreases in synaptic cell adhesion protein N-cadherin (*CDH2*) have previously been reported in AD temporal cortex (Ando et al., 2011). Therefore, upregulation of *CDH2* in this subpopulation of AD oligodendrocytes is an interesting discovery and may reflect a neuroprotective response to maintain contacts between axons and oligodendrocyte lineage cells (Schnädelbach et al., 2001). Cluster 2 AD oligodendrocytes upregulate pathways related to cholesterol metabolism. Cholesterol is an essential component of myelin (Saher et al., 2011), so identification of transcripts associated with cholesterol metabolism here (e.g., *FMO5* and *FDFT1*) is not surprising. However, in the context of AD, upregulation of these transcripts in an oligodendrocyte subpopulation may suggest neurosupportive and/or neurotoxic effects (Guttenplan et al., 2021). For example, conditional knockdown of squalene synthase (*FDFT1*), a rate-limiting enzyme in cholesterol synthesis, significantly delays myelination *in vivo* (Saher et al., 2005). However, high cholesterol level is also a risk factor for AD (Sheardown et al., 2011) and may exacerbate AD pathology by increasing A β production (as seen in APP/PS1 mice on a high-cholesterol diet) (Refolo et al., 2000) or A β aggregation (Yip et al., 2001). Clusters 0 and 2 AD oligodendrocytes downregulate pathways involved in amino acid synthesis (Figure S4C). Fatty acid synthesis by oligodendrocyte lineage cells is critical for both myelination and remyelination, as seen in acute lesions in a focal spinal cord demyelination model (Dimas et al., 2019). Decreased expression of stearoyl-CoA desaturase (*SCD*), a rate-limiting enzyme in monounsaturated fatty acid synthesis (Paton and Ntambi, 2009), in these oligodendrocytes may reflect a loss of function regarding endogenous fatty acid synthesis and could imply limited myelination/remyelination capabilities. Cluster 0, which makes up almost 80% of all oligodendrocytes identified in our snRNA-seq dataset, downregulates GO terms associated with synapse transmission, synaptic vesicle regulation, and ion transmembrane transport (Figure S4D). In contrast to cluster 1 AD oligodendrocytes, those in cluster 0 downregulate a number of synaptic cell adhesion molecules, such as E-cadherin (*CDH1*) (Kilinc, 2018), liprin- α (*PPFIA2*) (Lie et al., 2018), and disrupted in schizophrenia 1 (*DISC1*) (Hattori et al., 2010), which suggests decreased contacts between oligodendrocytes and axons. Also, cluster 0 AD oligodendrocytes downregulate GO terms associated with metabolism (e.g., DEGs include *PDE8A*, *PDE10A*, *PDE1A*, *CNP*, and *RORA*). Inhibition of phosphodiesterases (PDEs), a group of enzymes that regulate cyclic nucleotide cAMP and cGMP levels, is used in the treatment for cardiovascular diseases, inflammatory airway diseases, and erectile dysfunction (Boswell-Smith et al., 2006) and has been evaluated as a therapy for AD (Prickaerts et al., 2017; Wu et al., 2018). In addition to the potential broader cognitive improvement by PDE inhibition, downregulation of PDEs (specifically PDE4) promotes oligodendrocyte lineage cell differentiation and remyelination in a focal demyelination model (Syed et al., 2013), suggesting that these transcriptomic changes may serve a neuroprotective role in this specific oligodendrocyte subpopulation. We therefore hypothesized that some AD-associated transcriptional and functional changes in oligodendrocytes may also arise in other degenerative diseases, such as multiple sclerosis—even if the entire complement of transcriptional changes is not the same.

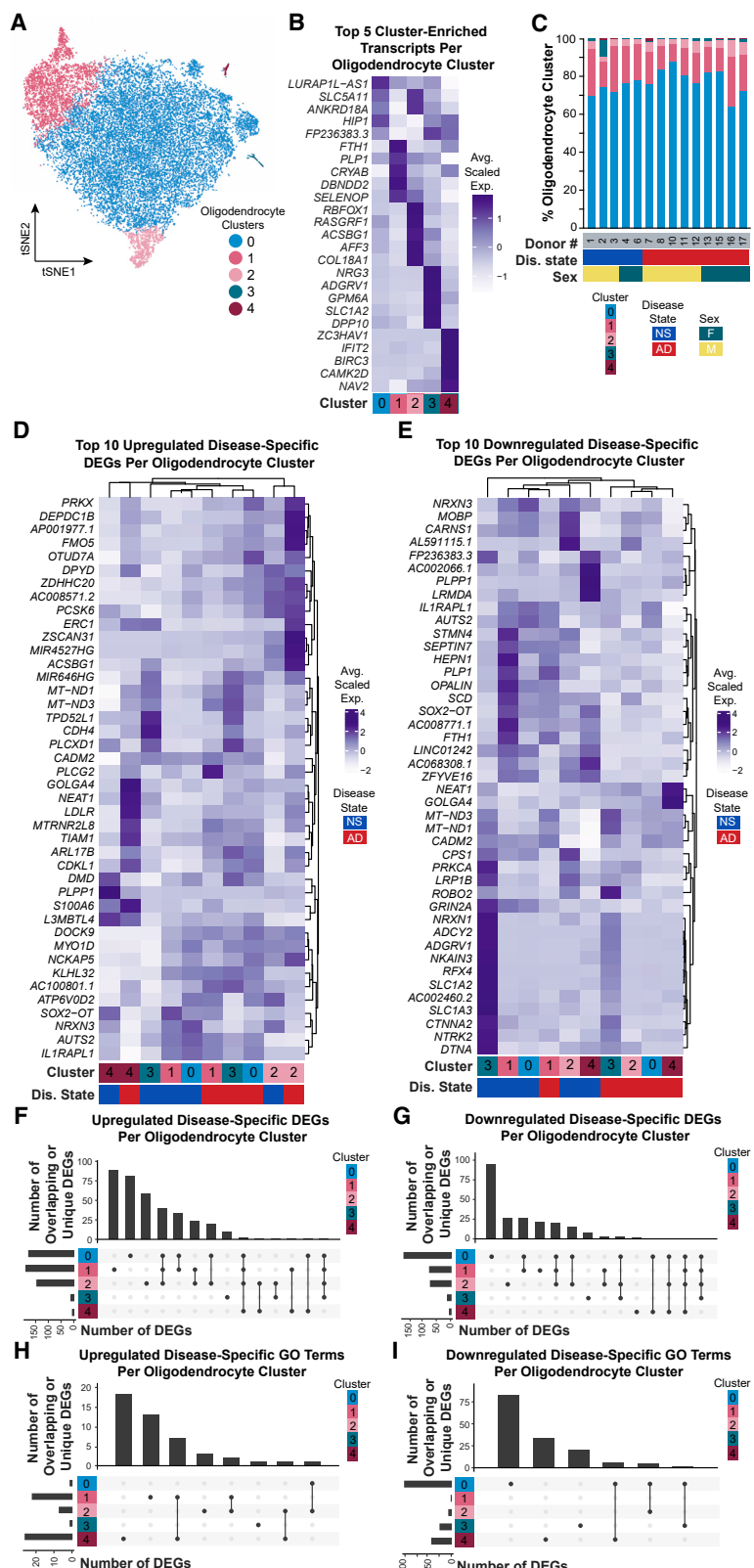


Figure 2. Oligodendrocytes are minimally heterogeneous but have cluster-specific transcriptomic changes in Alzheimer's disease

(A and B) (A) tSNE plot of oligodendrocyte nuclei ($N = 23,840$) and (B) corresponding average scaled expression heatmap of top-5 enriched/unique transcripts per cluster.

(C) Proportion of oligodendrocyte clusters identified in each donor.

Additional donor metavariables highlighted include disease state (blue, NS; red, AD) and sex (green, female; yellow, male).

(D and E) Average scaled expression of the top-10 (D) upregulated and (E) downregulated disease-specific DEGs split by cluster.

(F–I) UpSetR plots highlighting (F) upregulated DEGs, (G) downregulated DEGs, (H) upregulated GO terms, and (I) downregulated GO terms that are unique to or shared between clusters. Bars show number of DEGs per cluster (colored at left). Lines between clusters highlight shared DEGs. Abbreviations: AD, Alzheimer's disease; D#, donor number; DEG, differentially expressed gene; Dis., disease; F, female; GO, gene ontology; M, male; and NS, non-symptomatic. See also Figures S4 and S5.

Integration of oligodendrocytes from multiple datasets recovers overlapping subtypes

Given the abundance of high-quality, well-powered AD patient oligodendrocyte snRNA-seq datasets in the literature (Del-Aguila et al., 2019; Gerrits et al., 2021; Grubman et al., 2019; Leng et al., 2021; Mathys et al., 2019; Zhou et al., 2020), we next sought to determine whether we could resolve the same transcriptomic differences previously reported. We evaluated oligodendrocyte subtypes in each individual dataset and compared them with ours (Table S1; Figures S3I and S6–S8). By analyzing each dataset in isolation, we identified 5 oligodendrocyte clusters (M0–M4) in the Mathys dataset, 4 oligodendrocyte clusters (G0–G3) in the Grubman dataset, and 10 oligodendrocyte clusters (Z0–Z9) in the Zhou dataset (Figures 3A and 3B; Table S1). Using our oligodendrocyte subpopulation profiles as a reference (from now on, referred to as oligodendrocyte clusters S0–S4), we identified subpopulations that were also recognizable in the individual datasets. This included S1-like oligodendrocytes (clusters M0, M3, G0, and G3; defined by high expression of *FTH1*, *CRYAB*, *CNP*, and *FRY*) and S2-like oligodendrocytes (clusters M2 and G1; defined by *RBFOX1*, *RASGRF1*, *ACTN2*, and *SYNJ2*). In the Grubman dataset, we also identified S4-like oligodendrocytes (cluster G2; which highly expresses *S100A6*, *ITPKB*, and *NEAT1*). The remaining oligodendrocyte clusters in the Mathys dataset were defined by either no highly unique transcripts (cluster M1; only enriched transcript is X chromosome gene *XIST*, even though donors of both sex are represented in this cluster) or significantly fewer genes/UMI counts per nucleus compared with other clusters (cluster M4). In contrast, we identified twice as many oligodendrocyte subpopulations in the Zhou dataset compared with ours. However, although we detected more transcriptomically definable oligodendrocyte subpopulations, many of these clusters reflect gradations of transcript expression across multiple clusters. For example, oligodendrocyte clusters Z2, Z5, and Z9 express increasing levels of *PLP1*, *CNP*, *CNTN1*, *FRY*, and *KCNIP4* (similar to S1 oligodendrocytes), and oligodendrocyte clusters Z4 and Z7 express *ACTN2I*, *DTNA*, *RASGRF1*, and *RASGRF2* (similar to S2 oligodendrocytes). Overall, we found that 3 out of 5 subpopulations were present in the Zhou dataset (spread over 7 clusters). The remaining three clusters either were defined by higher mitochondrial transcript expression and low gene/UMI counts per nucleus (cluster Z3) or had uniquely identified profiles that do not have a corresponding profile in our snRNA-seq dataset.

In addition to evaluating oligodendrocytes from published datasets in isolation, we also integrated these datasets with ours. By doing so, we defined 7 oligodendrocyte subpopulations (clusters Int0–Int6) and found highly consistent representation of clusters from each dataset (Figures 3C and 3D; Table S5). To determine whether all datasets equally contributed to cluster-defining transcript expression, we evaluated the top-five integrated-oligodendrocyte-cluster-enriched transcripts by cluster and dataset (Figure 3E). Overall, 5 out of 7 integrated oligodendrocyte clusters were well defined across all datasets (clusters Int1 and Int3–Int6). Oligodendrocyte cluster Int0 was unremarkably defined (i.e., lacked unique or highly enriched transcript features) across all datasets. Comparing transcriptomic profiles between integrated oligodendrocyte clusters with our oligodendrocyte dataset, two

clusters had a high degree of similarity. Oligodendrocyte cluster Int0 expresses *SVEP1* and *PLXDC2* (similar to S0 oligodendrocytes), and Int6 oligodendrocytes express *NRP2*, *LUCAT1*, and *CAMK2D* (similar to S4 oligodendrocytes). In contrast to these oligodendrocyte subpopulations, in the integrated dataset, we identified two pairs of clusters in which expression gradation of transcripts was now well definable across all datasets (and not just in the Zhou dataset). Specifically, clusters Int1 and Int4 share expression of transcripts *FTH1*, *PLP1*, *APOD*, and *DBNDD2*. In addition, Int4 oligodendrocytes highly expresses *SGCZ*, *MDGA2*, *CNTN1*, *KCNIP4*, and *FRY* (which we identified in S1 oligodendrocytes).

Transcriptionally distinct astrocyte subtypes are independent of disease state

Following our investigation into oligodendrocyte gene expression changes, we next investigated our captured astrocytes. We sought to determine whether the increased numbers enabled us to detect novel subpopulations that had previously been missed. We identified 9 astrocyte subpopulations with unique transcriptomic signatures (Figures 4A and 4B) and also evaluated them by GO/pathway analysis to infer potential biological relevance (Table S6). For example, astrocyte clusters 0, 4, and 8 express unique sets of transcripts involved in synapse assembly, organization, and transmission (cluster 0: *EGFR*, *LRRC4C*, and *EPHB1*; cluster 4: *DCLK1*, *NTNG1*, and several semaphorins; cluster 8: *EPHA4*, *AKAP12*, and *NLGN4X*). Astrocyte clusters 4 and 6 highly express transcripts involved in glutamate signaling (*GRIA1*, *GRIK4*, and *SHISA6*). Clusters 2 and 5 express transcripts involved in extracellular matrix organization (cluster 2: *ADAMTSL3* and *L3MBTL4*; cluster 5: *ADAMTSL3* and *FBN1*), whereas cluster 5 also expresses transcripts involved in actin cytoskeletal organization (*SORBS1* and *SPIRE1*). The inclusion of *ADAMTSL3* in clusters 2 and 5 may point to a protective role of (some) AD or aged astrocytes, as their protective role has been reported in ischemia and cerebrovascular integrity in the APP/PS1 mouse model of AD (Cao et al., 2019). In contrast, cluster 3 astrocytes express transcripts involved in acute inflammatory responses (e.g., *SERPINA3*, *C3*, and *OSMR*) that we have reported on previously in both mice (Hasel et al., 2021; Liddelow et al., 2017) and humans (Barbar et al., 2020). Astrocyte cluster 1 is highly enriched for transcripts involved in oxidative stress (*PSAP*, *COX1*, and *ND1/3*) and associated with A β trafficking (e.g., *APOE* and *CLU*) and processing (e.g., *ITM2B/2C*). The inclusion of AD-risk genes, *APOE* and *CLU*, with integral membrane protein (*ITM2B/2C*) genes associated with cerebral amyloid angiopathy (Nelson et al., 2013; Vidal et al., 1999) in the same astrocyte cluster suggests a putative interaction. Astrocyte clusters 1 and 6 are both enriched in a number of metallothioneins and other transcripts involved in response to metal ions. Finally, cluster 7 expresses transcripts associated with apoptotic signaling and response to DNA damage. Most importantly, we did not identify any donor that singularly drove the identification of an astrocyte cluster (Figures S3A and S3F; see Figure S3A for the rationale of why two donors were removed from final analyses). Similar to our oligodendrocyte populations, astrocyte heterogeneity was not driven by any definable underlying sample variable, including disease state, sex, RNA quality, age of donor, or PMI.

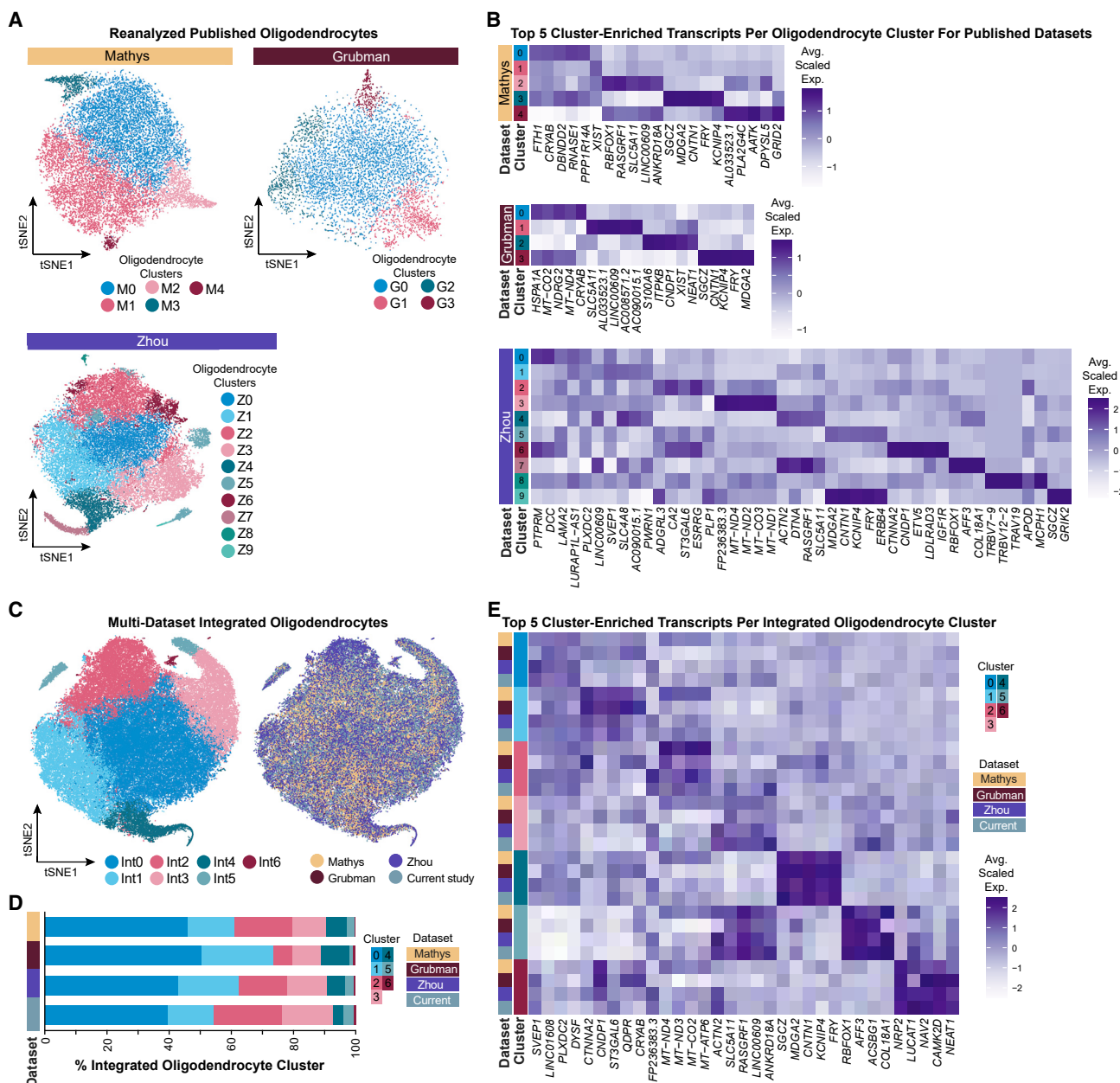


Figure 3. Integration of oligodendrocytes from multiple datasets reveals consistent identification of oligodendrocyte subtypes

(A and B) (A) tSNE plots of reanalyzed oligodendrocytes from published snRNA-seq datasets (Mathys, N = 18,229; Grubman, N = 7,604; Zhou, N = 34,949) and (B) their corresponding average scaled expression heatmap of the top 5 cluster-enriched/unique transcripts per cluster for each dataset.

(C) tSNE plots of integrated oligodendrocytes (N = 84,622) visualized by cluster (left) and by dataset (right).

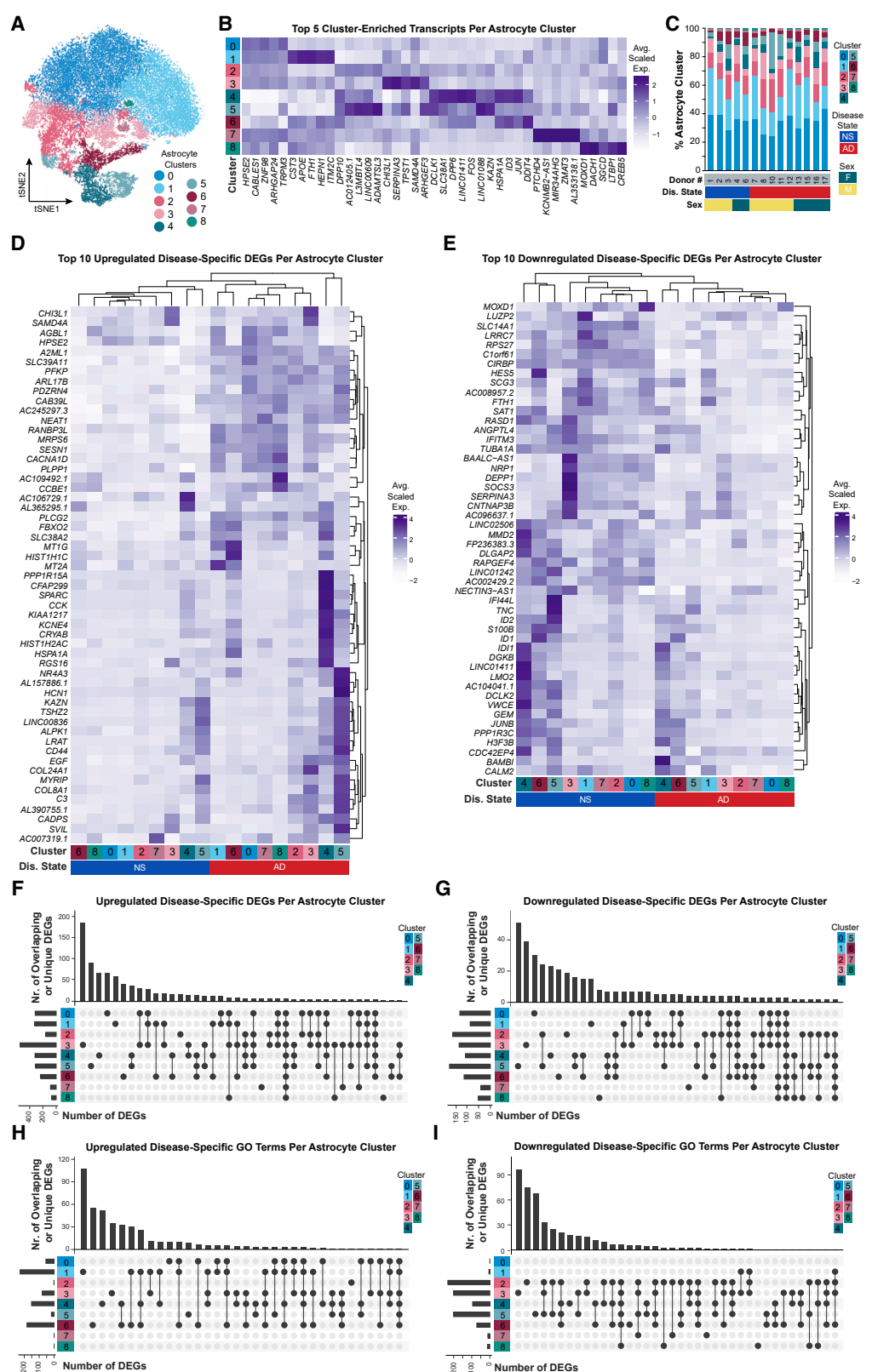
(D) Proportion of integrated clusters split by dataset.

(E) Average scaled expression heatmap of top 5 integrated-oligodendrocyte-cluster-enriched/unique transcripts by cluster and by dataset. See also Figures S6–S8 and S13.

Astrocytes have both common and cluster-specific transcriptomic changes in AD

We next analyzed samples for AD-associated differential gene expression and identified both common and cluster-specific transcriptomic changes between AD and NS astrocytes. In total, we identified 1,084 unique upregulated DEGs and 450 unique

downregulated DEGs between astrocyte clusters that were presumably driven by AD (Table S6). When comparing the top-10 up-/downregulated DEGs by cluster and disease state through hierarchical clustering, all AD and NS astrocyte subpopulations clustered separately (Figures 4D and 4E). Across all clusters, AD astrocytes upregulate transcripts including *HPSE2*, *SLC39A11*,



(legend on next page)

PFKP, *NEAT1*, *RANBP3L*, *PLPP1*, and *PLCG2*. *HPSE2*, a heparanase homolog, antagonizes heparanase activity (e.g., degradation of heparan sulfate proteoglycans in the extracellular matrix—important for removal of A β deposits that can aggregate with heparan sulfates [Lorente-Gea et al., 2017; O'Callaghan et al., 2008]). Given that *HPSE2* acts as a competitive inhibitor of *HPSE*, increased *HPSE2* release by astrocytes may enable expansion of A β deposits (Lorente-Gea et al., 2017), and therefore, inhibition of astrocyte-produced *HPSE2* may provide therapeutic benefit. *NEAT1* (nuclear enriched abundant transcript 1) is also an enticing target for future investigation as it is upregulated in several mouse models of AD, including APP/PS1 mice, and is putatively associated with regulation of *PINK1* degradation and impaired mitophagy (Huang et al., 2020). Additionally, across all clusters, AD astrocytes downregulate transcripts including *SLC14A1*, *C1orf61*, *CIRBP*, and *SAT1*. Some of these transcripts have important putative protective roles in neurodegenerative disease, so their decreased expression levels could be problematic. For instance, catabolic polyamine enzyme spermidine/spermine N1-acetyltransferase 1 (*SAT1*) levels are reduced by treatment with the diminazene aceteturate drug Berenil, which leads to worsened pathology in patients with Parkinson's disease (Lewandowski et al., 2010). In contrast to these pan-astrocytic DEGs, we also identified DEGs that were unique to single or combinations of astrocyte clusters (Figures 4F and 4G) and evaluated these gene sets by GO/pathway analysis (Figures 4H and 4I). By doing so, we were able to contextualize transcriptomic expression differences between AD and NS astrocytes in a cluster-specific manner and ultimately infer the potential biological role of astrocyte subpopulations in AD.

Astrocytes have both putative gain and loss of function in AD

We next evaluated astrocyte-cluster-specific “GO descriptions” associated with either upregulated or downregulated pathways (Figures 5, S9, and S10; Table S6). Cluster 1 AD astrocytes upregulate GO terms associated with cell death and oxidative stress (Figure 5A, e.g., regulator of cell cycle (*RGCC*), *PRDX1*, and *DDIT4*). *RGCC*, previously reported as upregulated in AD patients (Counts and Mufson, 2017), may be important for the reentry of postmitotic astrocytes to the cell cycle to enable proliferation around regions of pathology/degeneration. In comparison, peroxiredoxin (*PRDX1*), which is increased in AD patient hippocampi at the protein level (Chang et al., 2014), may have important antioxidant protection functions, suggesting a supportive role of these astrocytes in AD. Cluster 5 AD astrocytes upregulate pathways related to lipid storage and fatty acid oxidation (Figure 5B, e.g., *C3*, *ABCA1*, *PPARGC1*, *ACACB*). We, and others, have reported upregulation of complement component 3 (*C3*) in a specific

substate of reactive astrocytes that respond to inflammation in a range of neurodegenerative diseases (Diaz-Castro et al., 2019; Guttenplan et al., 2020; Liddelow et al., 2017; Shi et al., 2017), including AD (Liddelow et al., 2017) and AD mouse models (Lian et al., 2016; Wu et al., 2019). C3 $^{+}$ astrocytes are associated with a neurotoxic function and are only found in regions of neurodegeneration. As such, their inclusion here is not surprising given that we completed pathological analysis and snRNA-seq on regions with high pathology load. We performed immunofluorescent quantification of C3 $^{+}$ astrocytes in NS and AD patient samples and reported no difference at the protein level (Figure S11), though this may be a result of a reported increase in C3 $^{+}$ astrocytes with normal aging (Boisvert et al., 2018; Clarke et al., 2018), broader transcription versus translation differences between gene expression and protein levels, or the fact that these DEGs are specific to only a few subtypes of astrocytes in our dataset, and therefore, quantifying samples using single markers poses difficulties as it is unclear whether these astrocytes belong to the subtypes under investigation. We also quantified another cluster 5 DEG, *SPARC*, and reported no difference in the number of *SPARC* $^{+}$ /*GFAP* $^{+}$ cells or overall fluorescence intensity between NS and AD patient cortex (Figure S11), which—given our sequencing of astrocyte nuclei from prefrontal cortex—may also be a result of reported upregulation of *SPARC* in cortical astrocytes with normal aging (Clarke et al., 2018). Clusters 0, 1, 4, and 6 AD astrocytes share upregulation of pathways involved in response to metal ions (Figure S9A). DEGs associated with these GO terms include features that are cluster specific (e.g., *PRKN* in cluster 0) as well as those that are shared by multiple clusters (e.g., *DUSP1* in clusters 4 and 6; *MT1G* in clusters 0, 1, 4, and 6). Upregulation of *DUSP1* (dual-specificity phosphatase, also known as mitogen-activated protein kinase, MKP1) has previously been reported in models of Parkinson's disease (Collins et al., 2013) and Huntington's disease (Taylor et al., 2013), as well as following ischemic stroke (Boutros et al., 2008; Ramsay et al., 2019) and seizures (Kedmi and Orr-Urtreger, 2007). *DUSP1* upregulation is associated with repression of apoptosis and neuronal cell death pathways in neuroblastoma (Nunes-Xavier et al., 2019), suggesting another putatively important protective response in astrocyte subpopulations in AD. Clusters 4 and 6 AD astrocytes also share upregulation of protein folding/unfolding pathways (e.g., DEGs include *HSPA1B*, *DNAJB1*, and *ATF3I*; Figure S9A), as well as downregulation of signaling receptor activity and axonal guidance pathways (e.g., *GRIA1* and *NLGN1*; Figure S9B). Increased expression of activating transcription factor 3 (*ATF3*) suggests a response to endoplasmic reticulum stress, a pathway that propagates through the induction of eukaryotic initiation factor 2 (eIF2) kinase-associated genes (Jiang et al., 2004). In addition, since these astrocyte clusters downregulate transcripts critical for both synaptogenesis and

Figure 4. Astrocytes are heterogeneous and have both common and cluster-specific transcriptomic changes in Alzheimer's disease

(A and B) (A) tSNE plot of astrocyte nuclei (N = 41,071) and (B) corresponding average scaled expression heatmap of top 5 enriched/unique transcripts per cluster. (C) Proportion of astrocyte clusters identified in each donor. Additional donor metavariables highlighted include disease state (blue, NS donors; red, AD donors) and sex (green, female; yellow, male). (D and E) Average scaled expression of the top-10 (D) upregulated and (E) downregulated disease-specific DEGs split by cluster. (F–I) UpSetR plots highlighting (F) upregulated DEGs, (G) downregulated DEGs, (H) upregulated GO terms, and (I) downregulated GO terms that are unique to or shared between clusters. Abbreviations: AD, Alzheimer's disease; D#, donor number; DEG, differentially expressed gene; Dis., disease; F, female; GO, gene ontology; M, male; and NS, non-symptomatic. See also Figure S11.

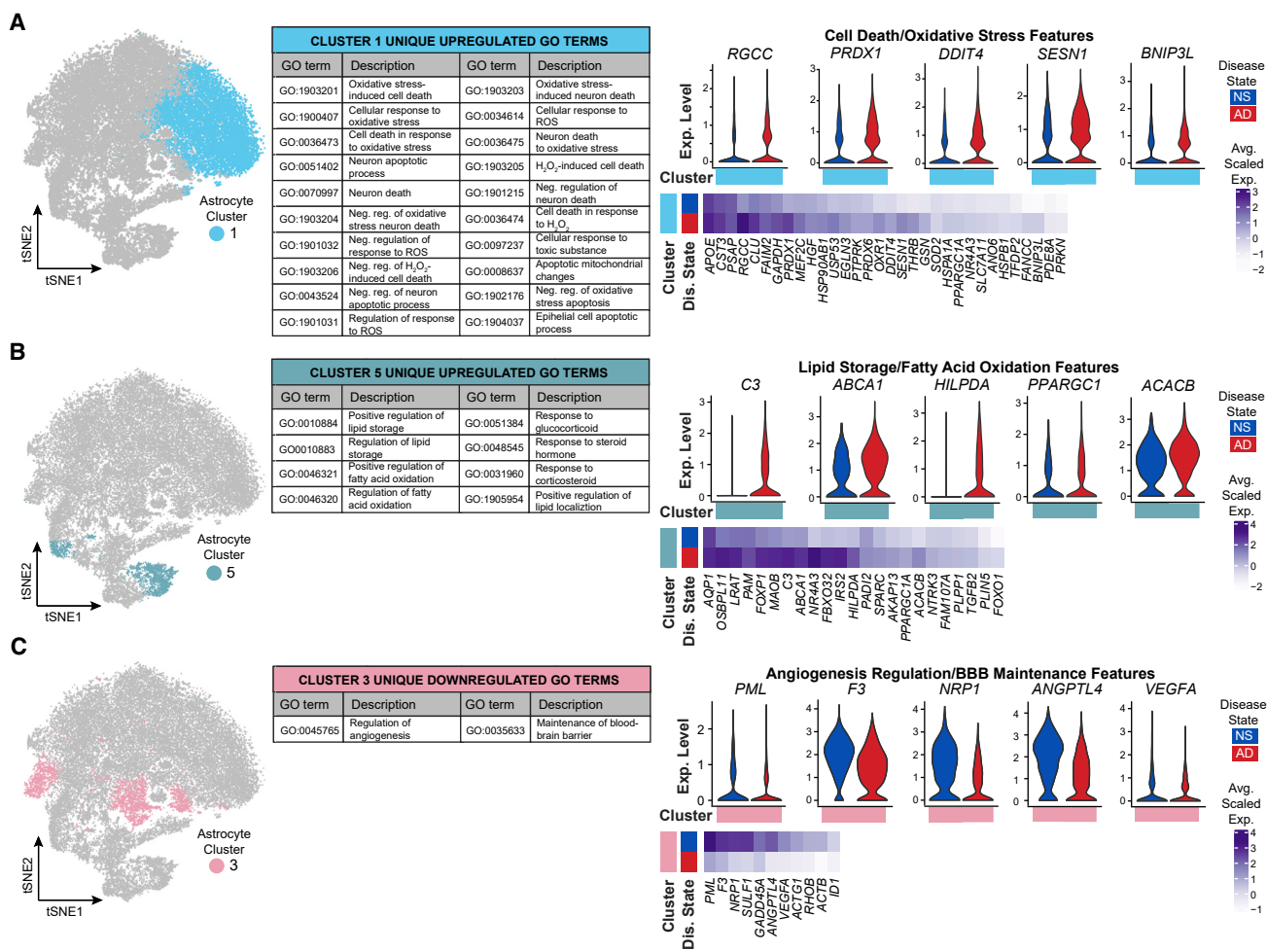


Figure 5. Astrocyte transcriptomic profiles suggest cluster-specific gain and loss of functional changes in Alzheimer's disease

tSNE plots highlighting several clusters of interest, unique/shared GO terms, and DEGs associated with GO terms. GO-associated DEGs are presented as average scaled expression heatmaps by cluster of interest and split by disease state (blue, NS donors; red, AD donors). DEGs are highlighted on violin plots to resolve the range of expression (log normalized UMI counts) across all astrocytes in single or multiple clusters.

(A) Upregulated cell death and oxidative stress features unique to cluster 1.

(B) Upregulated lipid storage and fatty acid oxidation features unique to cluster 5.

(C) Downregulation of angiogenesis regulation and blood-brain barrier maintenance features unique to cluster 3. Abbreviations: AD, Alzheimer's disease; BBB, blood-brain barrier; DEG, differentially expressed genes; Dep., dependent; Dis., disease; GO, gene ontology; H₂O₂, hydrogen peroxide; Neg., negative; NS, non-symptomatic; Reg., regulation; ROS, reactive oxygen species; and UMI, unique molecular identifier. See also Figures S9–S11.

astrocyte morphogenesis (such as neuroligin-1, *NLG1*), this may implicate that putative decreased synaptic maintenance functions could be due to stunted/altered astrocyte territories and limited infiltration of surrounding neuropil (Stogsdill et al., 2017). The intersection of unfolding protein response (UPR) and synaptic maintenance mechanisms was recently evaluated by Smith et al., who found that chronic PERK-eIF α signaling in astrocytes induced an UPR-associated reactivity state in which astrocytes lose synaptic support functions and ultimately induce neuron death *in vitro* and in prion infection in mice (Smith et al., 2020). Cluster 3 AD astrocytes downregulate GO terms associated with angiogenesis regulation and BBB maintenance (Figure 5C). As a key modulator of vascular permeability and angiogenesis, downregulation of vascular endothelial growth factor A (VEGFA) may be a

protective astrocyte response to limit BBB breakdown. Administration of human recombinant VEGF₁₆₅ 1 h post-ischemic stroke exacerbated BBB leakage in a middle cerebral artery occlusion rat model (Zhang et al., 2000) and inhibition of VEGFA improved BBB integrity around active lesions in an experimental autoimmune encephalomyelitis mouse model, decreasing immune cell infiltration and reducing overall demyelination (Argaw et al., 2012).

Astrocyte subtypes are regionally heterogeneous in humans and mice

Given recent discoveries highlighting astrocytes as increasingly variable across the CNS (Bayraktar et al., 2020), we next sought to explore whether our heterogeneous astrocyte subtypes reside in different cortical locations. However, examining regional

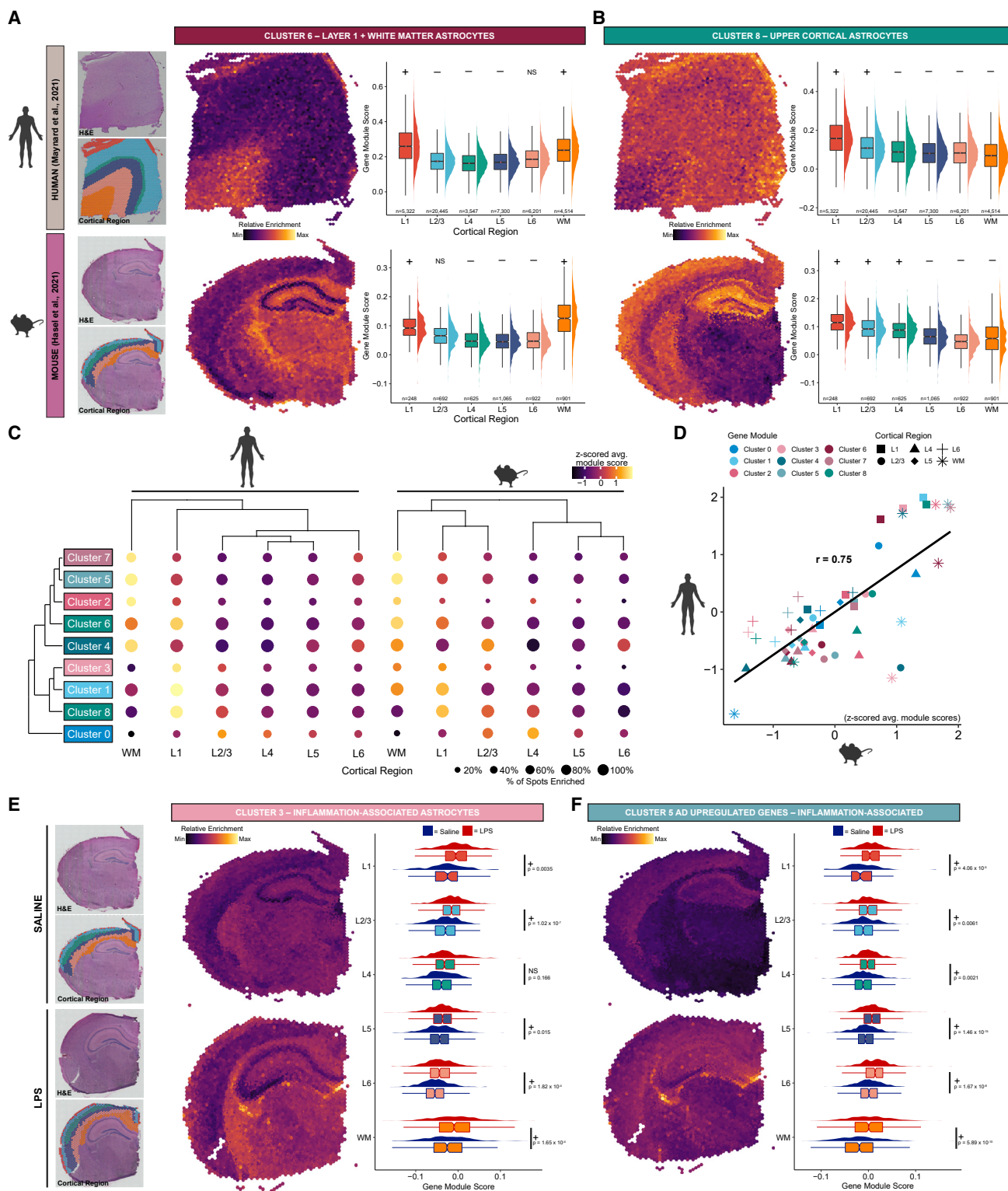


Figure 6. Astrocyte subtypes are regionally heterogeneous

(A and B) Visualization and differential enrichment results for cluster 6 marker genes enriched in layer 1 and white matter (A), and cluster 8 genes enriched in the upper layers of the cortex (B). For both, upper: human spatial transcriptomics data from Maynard et al. (2021). Lower: mouse spatial transcriptomics data from Hasel et al. (2021). (Leftmost) H&E staining and regional annotation of spots from the representative Visium section. Relative enrichment of cluster gene module section, and box and density plots of gene module scores across all spots and all sections grouped by cortical region for clusters 6 and 8. Cluster gene modules (legend continued on next page)

differences in these astrocyte subtypes or disease-associated reactive substates is a challenging prospect given that many clusters are defined by slight differences in the expression of dozens or hundreds of genes rather than the expression of individual DEGs specific to a single cluster, making it difficult to evaluate these gene signatures using traditional *in situ* methods. To overcome these challenges, we leveraged published spatial transcriptomics datasets to explore regional differences in our astrocyte subtypes in the NS human brain (Maynard et al., 2021) and compared this with the healthy and inflamed mouse brain (Hasel et al., 2021).

To determine the likely location of each astrocyte population, we created modules of marker genes from each cluster (Hasel et al., 2021; Tirosh et al., 2016) and examined the expression of the modules across the human and mouse spatial transcriptomics data (Figure S12A). We found that all astrocyte cluster modules exhibited significant differences in expression in at least one cortical layer (Kruskal-Wallis test, $p < 0.05$); however, there were large differences in the degree to which cluster gene signatures were region specific (Figure S12F). Some cluster modules were strongly enriched in select regions. For example, the cluster 6 gene signature is significantly enriched in layer 1 and the WM in both human and mouse brain (Figure 6A). Several cluster 6 marker genes, such as *ID1*, *ID3*, and *AGT*, have been previously reported in WM and L1 astrocytes in the mouse (Bayraktar et al., 2020), supporting this localization. Cluster 8, in contrast, was enriched in upper cortical layers L1–L3 in both species (Figure 6B), fitting with the recent description of several genes in this set having elevated expression in upper cortical astrocytes, such as *GRM3*, *SLCO1C1*, and *EPHB1* (Bayraktar et al., 2020). In aggregate, we found significant heterogeneity in the cortical regions most enriched for each astrocyte cluster (Figure 6C; Figure S12G). Regional cluster enrichment was similar between the human and mouse datasets, supporting the robustness of the gene module approach and suggesting that the astrocyte subtypes we identified may be conserved between species (Figure 6D).

Cluster 3 astrocytes were denoted by several genes previously described as upregulated in response to acute inflammation. Correspondingly, this was less well defined in the NS human and healthy mouse brain (Figure S12G) as compared with the inflamed mouse brain where this gene signature was upregulated across nearly all cortical regions (Figure 6E). This may indicate that cluster 3 astrocytes are not region specific but rather gener-

ally associated with inflammation. To explore whether some of the AD-associated gene expression changes in each astrocyte subtype may also be associated with inflammation, we next compared the expression of AD gene modules for each cluster between the healthy and inflamed mouse brain. We found that the cluster 5 AD module was upregulated across all cortical layers in the inflamed mouse brain (Figure 6F), suggesting these AD-associated gene expression changes may be attributable to inflammatory mechanisms. Notably, AD gene signatures for nearly all other astrocyte clusters were not significantly enriched in the inflamed mouse brain relative to the healthy control brain (Figure S12H), indicating non-inflammatory mechanisms may be responsible for these changes.

Data integration increases astrocyte numbers and enables consistent identification of unique subpopulations

Although we defined 9 transcriptomically distinct astrocyte clusters in our snRNA-seq dataset (from now on, referred to as astrocyte clusters S0–S8), when reanalyzing published astrocyte datasets in isolation, we identified 5 clusters (M0–M4) in the Mathys dataset, 5 clusters (G0–G4) in the Grubman dataset, and 7 clusters (Z0–Z6) in the Zhou dataset (Figures 7A and 7B; Table S1). With our dataset serving as a reference, we identified one or two previously defined astrocyte subpopulations in the Mathys and Grubman datasets: S1-like astrocytes (clusters M0, G1; which are defined by high expression of *CST3*, *FTH1*, *APOE*, and *ITM2C*) and S0-like astrocytes (cluster G0; which highly expresses *CACNB2*, *GPC5*, and *RORA*). In contrast to the Mathys and Grubman datasets, we identified 6 out of 9 astrocyte subpopulations in the Zhou dataset, which were similar to S0–S5 astrocytes. Similar to with our astrocyte snRNA-seq dataset, we did not identify any singular sample variable that was exclusively associated with a single astrocyte cluster across all three datasets (Figure S7). This is in contrast with original findings presented in Grubman et al. (2019), which reported differences in the proportion of astrocyte clusters between AD and NS patients. However, we believe these detected differences may stem from the lack of sample integration.

Cross-comparing astrocyte subpopulation profiles between datasets is a useful exercise to evaluate what potential similarities and differences exist. In doing so, we defined 9 astrocyte subpopulations (referred to as astrocyte clusters Int0–Int8) (Figure 7C) and found that these astrocyte subpopulations had

were significantly enriched (+) or de-enriched (-) in spots from the indicated region compared with the rest of the cortex (Wilcoxon rank-sum test with Bonferroni correction).

(C) Summary dot plot of astrocyte cluster gene modules across human (left) and mouse (right) cortical regions. Dots colored by Z-scored average gene module score. Dot sizes correspond to the percentage of spots with a gene module score greater than zero, indicating elevated expression of the gene set compared with control gene sets (see STAR Methods).

(D) Scatter plot comparing Z-scored average gene module scores across regions and clusters between humans and mice, showing cluster module enrichment is similar. A linear regression line is shown (r refers to Pearson's r correlation coefficient).

(E) Relative enrichment of cluster 3 module overlaid on saline (upper) and LPS (lower) sections. Box and density plot comparing expression of cluster 3 module across spots in LPS- versus saline-injected mice (right).

(F) Relative enrichment of genes upregulated in cluster 8 in AD overlaid on saline (top) and LPS (bottom) sections. Box and density plot comparing expression of cluster 8 AD module across cortical regions in LPS- versus saline-injected mice (right). For (E and F) +/- symbol represents whether the cluster 3 module is significantly upregulated or downregulated in spots from the indicated region in LPS- versus saline-injected mice (Wilcoxon rank-sum test with Bonferroni correction). See Table S7 for test statistics and p-values. Abbreviations: AD, Alzheimer's disease; NS, non-significant; H&E, hematoxylin and eosin; and LPS, lipopolysaccharide. See also Figure S12.

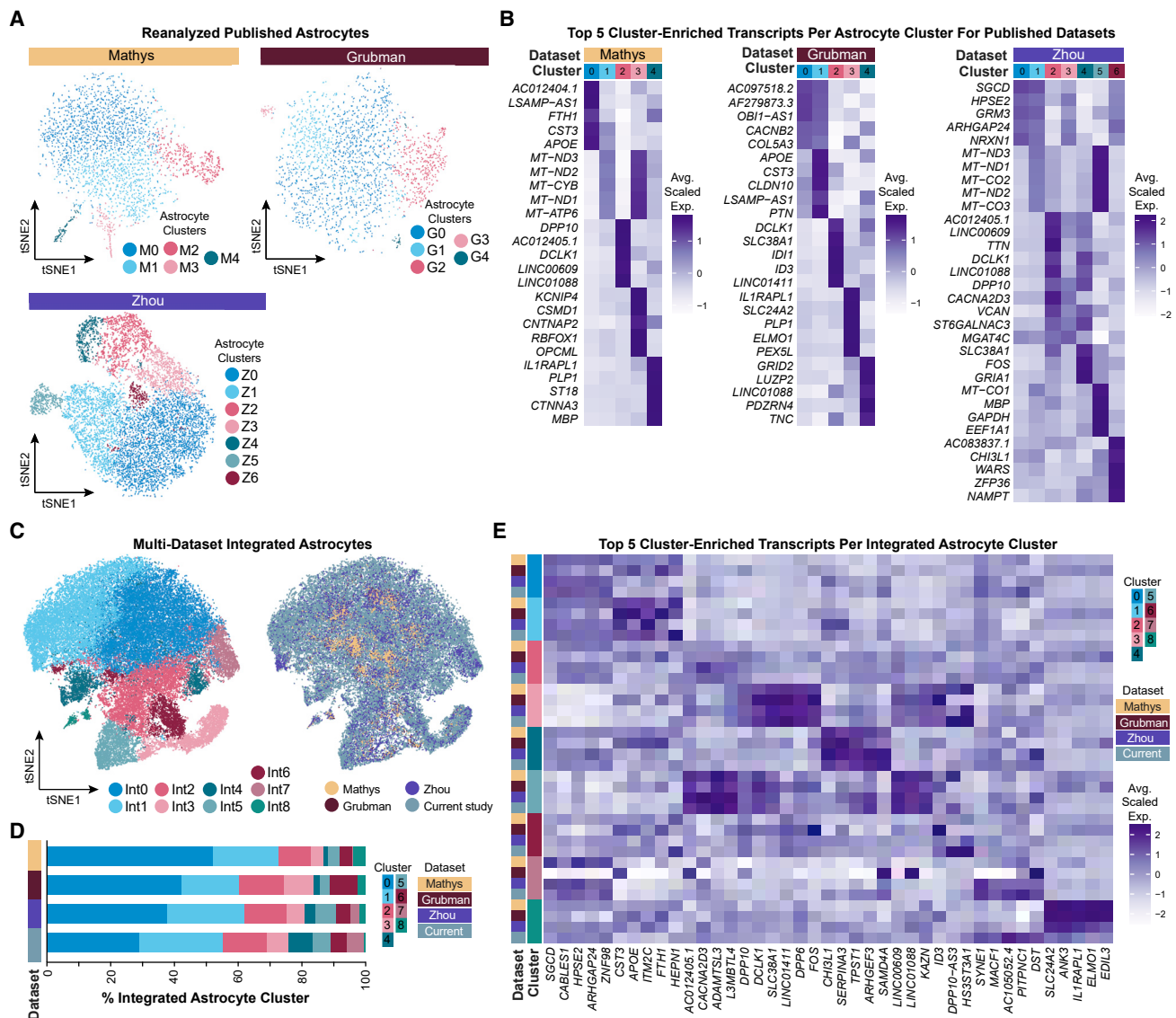


Figure 7. Integrating astrocyte snRNA-seq datasets allows for improved resolution of unique astrocyte subpopulations

(A and B) (A) tSNE plots of reanalyzed astrocytes from published snRNA-seq AD datasets (Mathys, N = 3,079; Grubman, N = 2,330; Zhou, N = 10,538) and (B) their corresponding average scaled expression heatmap of the top 5 cluster-enriched/unique transcripts.

(C) tSNE plots of integrated astrocytes (N = 57,018) as visualized by cluster (left) and by dataset (right). Mathys data are in yellow, Grubman data are in dark red, Zhou data are in violet, and this study's data are in steel blue.

(D) Proportion of integrated astrocyte clusters identified in the integrated dataset.

(E) Average scaled expression heatmap of top-5 integrated-astrocyte-cluster-enriched/unique transcripts by cluster and by dataset. See also Figures S1, S3, S6–S8, and S13.

markedly similar proportions in each dataset (Figures 7C and 7D; Table S5). This is exciting as it highlights the feasibility of improving subpopulation identification post hoc via data integration, thereby overcoming limitations in the total number of astrocytes captured and depth of sequencing levels in individual datasets (Figure S8A). To determine whether all datasets equally contributed to cluster-defining transcript expression, we evaluated the top-five integrated-astrocyte-cluster-enriched transcripts by cluster and dataset (Figure 7E). Remarkably, 7 out of 9 integrated clusters were well defined across all datasets (clus-

ters Int0–Int6), and their corresponding transcriptomic profiles were similar to those of S0–S6 astrocytes. In contrast, cluster Int7 defining features were primarily present in the Zhou dataset and our dataset, and its profile most resembles astrocyte cluster Int0. However, this cluster had lower total genes and UMIs identified per nucleus, which is likely why it was identified as unique. Additionally, cluster Int8 was primarily identified in Mathys, Grubman, and Zhou datasets, and its profile is defined by higher expression of oligodendrocyte-associated and mitochondrial transcripts.

This integration method enabled identification of unique astrocyte subpopulations not previously resolvable in published astrocyte datasets. Next, we explored whether AD-associated astrocyte transcriptional changes originally reported in each study were resolvable when integrating these datasets with ours (Figures S13A–S13D). Only the DEGs highlighted in the Zhou et al. dataset were detectable in the integrated dataset (upregulated, Z5/Int2; downregulated, Z2/Int5; Figure S13D), likely due to increased numbers of sequenced astrocytes. Other reported disease-associated astrocyte DEGs were not specific to individual integrated clusters. Conversely, reverse probing for previously described disease-associated oligodendrocyte-cluster-specific DEGs was more successful (Figures S13E–S13H).

This highlights that we can leverage large astrocyte datasets to better resolve astrocyte subpopulations in smaller datasets. For example, we were originally unable to detect a C3⁺ astrocyte subpopulation in both Mathys and Grubman datasets (Figure S11H). In comparison, we identified C3⁺ astrocytes in both our dataset (astrocyte clusters S3 and S5) and the Zhou dataset (astrocyte cluster Z2; however, this identification was driven by a single donor) (Tables S1 and S3). Once all datasets were evaluated together, this C3⁺ astrocyte subpopulation was uniquely ascribed to astrocyte clusters Int4 and Int5 (Figure S11G; Table S5), with all datasets contributing to C3 expression in astrocyte cluster Int4 and our dataset primarily contributing to C3 expression in astrocyte cluster Int5. This difference may be due to differences in pathological loads of the same samples being sequenced—as we previously reported, C3⁺ astrocytes are present only in high-pathology brain regions (Liddelow et al., 2017). Given the cluster-specific transcriptomic changes we identified between AD and NS patients, we believe that this underscores the importance of resolving these unique astrocyte subpopulations in the context of health and disease.

DISCUSSION

Here, we present a snRNA-seq dataset and paired pathology assessment resource for both astrocytes and oligodendrocytes from a well-defined human AD and age-matched NS patient cohort. This approach enabled us to identify putative biologically important astrocyte subpopulations. To localize these transcriptomically distinct populations of astrocytes, we profiled 10X Visium spatial transcriptomics datasets and localized astrocyte subgroups in both the human and mouse brain. In addition, by leveraging our astrocyte snRNA-seq dataset with published astrocyte snRNA-seq datasets, we identified unique and previously undefinable astrocyte subpopulations in all datasets.

Integral for the success of this resource, we limited donor genetic variance and characterized the pathology of donor tissue from the same sample as sequenced material. Given the spatial heterogeneity that can occur due to differences in disease pathology and progression in adjacent brain regions (Komarova and Thalhauser, 2011; Murray et al., 2011), we are enormous proponents of being self-critical about what is driving results throughout analyses—being particularly wary of outlier donors and/or donor features. For example, after the first round of analyzing our astrocyte snRNA-seq data, we identified one cluster that was entirely representative of a single donor (D5). When

evaluating this cluster, we found that it was highly enriched for transcripts associated with neuroinflammation and interferon gamma signaling (e.g., *IFIT-1/2/3/6*, *IFI-44/44L/H1*; see Figures S3A–S3E). Classified as a NS control, we double checked our pathology characterization, which corroborated this donor as seemingly NS due to very low pathology load. However, upon further investigation into clinical evaluations associated with this donor, we discovered D5 had vascular dementia. This unique astrocyte subpopulation shares remarkable similarity to an interferon-responsive subpopulation of neuroinflammatory reactive astrocytes following acute inflammation in mice and several neurodegenerative disease models, including AD, which we published recently (Hasel et al., 2021).

Although our dataset and integration with published datasets highlight novel and putative functional populations of glia in AD, future functional studies are required to evaluate these subpopulations and their potential for modulation by therapies. How heterogeneity of astrocyte and oligodendrocyte responses might differ with disease progression or other patient cohort characteristics, such as AD-associated mutations, secondary disease contraindications, or ethnic backgrounds, is an open question. Future human stem cell organoid and novel AD mouse models and isolated rodent cells used in *in vitro* functional testing will be able to address these questions. We also hope that continued integration of our data with future snRNA-seq and spatial datasets will add greater insight to these and many new questions.

STAR METHODS

Detailed methods are provided in the online version of this paper and include the following:

- KEY RESOURCE TABLE
- RESOURCE AVAILABILITY
 - Lead contact
 - Materials availability
 - Data and code availability
- EXPERIMENTAL MODEL AND SUBJECT DETAILS
 - Postmortem human cohorts
- METHOD DETAILS
 - Tissue RNA quality verification
 - APOE genotype verification
 - Immunohistochemistry and imaging of postmortem frozen human prefrontal cortex tissue
 - Isolation of nuclei from postmortem frozen human prefrontal cortex tissue
 - Fluorescence-activated cell sorting for astrocytic nuclei enrichment
 - snRNA-seq pipeline
 - snRNA-seq data analysis
 - Cluster-specific differential gene expression and pathway analysis
 - Reanalysis of previously published snRNA-seq and scRNA-seq datasets
 - Cell type-specific multi-dataset analyses
 - Analysis of previously published spatial transcriptomic data

- QUANTIFICATION AND STATISTICAL ANALYSIS
 - Statistics
- ADDITIONAL RESOURCES
 - Raw sequencing data

SUPPLEMENTAL INFORMATION

Supplemental information can be found online at <https://doi.org/10.1016/j.neuron.2022.03.008>.

ACKNOWLEDGMENTS

We thank members of the Liddelow lab for review of this manuscript. We also thank the Genome Technology Center at NYU Langone Medical Center for sequence alignment and data preprocessing, the Cytometry and Cell Sorting Laboratory at NYU Langone Medical Center for assistance in sorting samples, the Neuropathology Brain Bank & Research CoRE at the Icahn School of Medicine at Mount Sinai for preparing and staining all pathology samples, and the Experimental Pathology Research Laboratory for scanning all pathology samples. Donor samples were provided by the Brain Tissue Resource Center at Rhode Island Hospital, UCSD Alzheimer's Disease Center, and New York University Alzheimer's Disease Center (which is sponsored in part by PHS grant P30 AG08051). S.A.L. was supported by NYU School of Medicine, the Blas Frangione Foundation, the Neurodegenerative Diseases Consortium from MD Anderson, Alzheimer's Research UK, the Gifford Family Neuroimmune Consortium as part of the Cure Alzheimer's Fund, the Alzheimer's Association, and generous anonymous donors. J.S.S. was supported by the National Institutes of Health (T32 via T32AG052909 [Wisniewski, Scharfman]). Additionally, S.A.L. and J.S.S. were supported by the Alzheimer's Disease Resource Center at NYU Langone Medical Center. A.F. was supported by the Alzheimer's Disease Resource Center at NYU Langone Medical Center (P30 AG066512 [Wisniewski]).

AUTHOR CONTRIBUTIONS

J.S.S., M.R.O., and P.H. conducted the experiments. J.S.S., M.R.O., P.H., and T.D. analyzed the data. J.S.S. and S.A.L. planned the experiments. J.S.S., M.R.O., and S.A.L. prepared the manuscript. All authors edited and approved the final version of the manuscript.

DECLARATIONS OF INTERESTS

S.A.L. is a founder of AstronauTx Ltd and a member of its scientific advisory board. All other authors declare no competing interests.

INCLUSION AND DIVERSITY

We worked to ensure sex balance in the selection of human samples. One or more of the authors of this paper self-identifies as a member of the LGBTQ+ community. One or more of the authors of this paper self-identifies as an underrepresented ethnic minority in science. While citing references scientifically relevant for this work, we also actively worked to promote gender balance in our reference list.

Received: March 22, 2021

Revised: January 24, 2022

Accepted: March 8, 2022

Published: April 4, 2022

REFERENCES

- Alzheimer's Association (2021). 2021 Alzheimer's disease facts and figures. *Alzheimers Dement.* **17**, 327–406. <https://doi.org/10.1002/alz.12328>.
- Amezquita, R.A., Lun, A.T.L., Becht, E., Carey, V.J., Carpp, L.N., Geistlinger, L., Marini, F., Rue-Albrecht, K., Risso, D., Soneson, C., et al. (2020). Orchestrating single-cell analysis with Bioconductor. *Nat. Methods* **17**, 137–145. <https://doi.org/10.1038/s41592-019-0654-x>.
- Ando, K., Uemura, K., Kuzuya, A., Maesako, M., Asada-Utsugi, M., Kubota, M., Aoyagi, N., Yoshioka, K., Okawa, K., Inoue, H., et al. (2011). N-cadherin regulates p38 MAPK signaling via association with JNK-associated leucine zipper protein: implications for neurodegeneration in Alzheimer disease. *J. Biol. Chem.* **286**, 7619–7628. <https://doi.org/10.1074/jbc.M110.158477>.
- Argaw, A.T., Asp, L., Zhang, J., Navrashina, K., Pham, T., Mariani, J.N., Mahase, S., Dutta, D.J., Seto, J., Kramer, E.G., et al. (2012). Astrocyte-derived VEGF-A drives blood-brain barrier disruption in CNS inflammatory disease. *J. Clin. Invest.* **122**, 2454–2468. <https://doi.org/10.1172/JCI60842>.
- Bankhead, P., Loughrey, M.B., Fernández, J.A., Dombrowski, Y., McArt, D.G., Dunne, P.D., McQuaid, S., Gray, R.T., Murray, L.J., Coleman, H.G., et al. (2017). QuPath: open source software for digital pathology image analysis. *Sci. Rep.* **7**, 16878. <https://doi.org/10.1038/s41598-017-17204-5>.
- Barbar, L., Jain, T., Zimmer, M., Kruglikov, I., Sadick, J.S., Wang, M., Kalpana, K., Rose, I.V.L., Burstein, S.R., Rusielewicz, T., et al. (2020). CD49f is a novel marker of functional and reactive human iPSC-derived astrocytes. *Neuron* **107**, 436–453.e12. <https://doi.org/10.1016/j.neuron.2020.05.014>.
- Bayraktar, O.A., Bartels, T., Holmqvist, S., Kleshchevnikov, V., Martirosyan, A., Polioudakis, D., Ben Haim, L., Young, A.M.H., Batiuk, M.Y., Prakash, K., et al. (2020). Astrocyte layers in the mammalian cerebral cortex revealed by a single-cell in situ transcriptomic map. *Nat. Neurosci.* **23**, 500–509.
- Boisvert, M.M., Erikson, G.A., Shokhirev, M.N., and Allen, N.J. (2018). The aging astrocyte transcriptome from multiple regions of the mouse brain. *Cell Rep.* **22**, 269–285. <https://doi.org/10.1016/j.celrep.2017.12.039>.
- Boswell-Smith, V., Spina, D., and Page, C.P. (2006). Phosphodiesterase inhibitors. *Br. J. Pharmacol.* **147** (suppl 1), S252–S257. <https://doi.org/10.1038/sj.bjp.0706495>.
- Boutros, T., Chevet, E., and Metrakos, P. (2008). Mitogen-activated protein (MAP) kinase/MAP kinase phosphatase regulation: roles in cell growth, death, and cancer. *Pharmacol. Rev.* **60**, 261–310. <https://doi.org/10.1124/pr.107.00106>.
- Cao, Y., Xu, H., Zhu, Y., Shi, M.J., Wei, L., Zhang, J., Cheng, S., Shi, Y., Tong, H., Kang, L., et al. (2019). ADAMTS13 maintains cerebrovascular integrity to ameliorate Alzheimer-like pathology. *PLoS Biol.* **17**, e3000313. <https://doi.org/10.1371/journal.pbio.3000313>.
- Carter, S.F., Schöll, M., Almkvist, O., Wall, A., Engler, H., Långström, B., and Nordberg, A. (2012). Evidence for astrocytosis in prodromal Alzheimer disease provided by ¹¹C-deuterium-L-depronyl: a multitracer PET paradigm combining ¹¹C-Pittsburgh compound B and ¹⁸F-FDG. *J. Nucl. Med.* **53**, 37–46. <https://doi.org/10.2967/jnumed.110.087031>.
- Chang, R.Y., Etheridge, N., Dodd, P.R., and Nouwens, A.S. (2014). Targeted quantitative analysis of synaptic proteins in Alzheimer's disease brain. *Neurochem. Int.* **75**, 66–75. <https://doi.org/10.1016/j.neuint.2014.05.011>.
- Clarke, L.E., Liddelow, S.A., Chakraborty, C., Münch, A.E., Heiman, M., and Barres, B.A. (2018). Normal aging induces A1-like astrocyte reactivity. *Proc. Natl. Acad. Sci. USA* **115**, E1896–E1905. <https://doi.org/10.1073/pnas.1800165115>.
- Collins, L.M., O'Keeffe, G.W., Long-Smith, C.M., Wyatt, S.L., Sullivan, A.M., Toulouse, A., and Nolan, Y.M. (2013). Mitogen-activated protein kinase phosphatase (MKP)-1 as a neuroprotective agent: promotion of the morphological development of midbrain dopaminergic neurons. *NeuroMolecular Med.* **15**, 435–446. <https://doi.org/10.1007/s12017-013-8230-5>.
- Counts, S.E., and Mufson, E.J. (2017). Regulator of cell cycle (RGCC) expression during the progression of Alzheimer's disease. *Cell Transplant.* **26**, 693–702. <https://doi.org/10.3727/096368916X694184>.
- Crowell, H.L., Soneson, C., Germain, P.-L., Calini, D., Collin, L., Raposo, C., Malhotra, D., and Robinson, M.D. (2019). *muscat* detects subpopulation-specific state transitions from multi-sample multi-condition single-cell transcriptomics data. *Nat. Commun.* **10**, 6077. <https://doi.org/10.1038/s41467-020-19894-4>.
- de la Torre, J.C. (2004). Is Alzheimer's disease a neurodegenerative or a vascular disorder? Data, dogma, and dialectics. *Lancet Neurol.* **3**, 184–190. [https://doi.org/10.1016/S1474-4422\(04\)00683-0](https://doi.org/10.1016/S1474-4422(04)00683-0).

- De Strooper, B., and Karran, E. (2016). The cellular phase of Alzheimer's disease. *Cell* 164, 603–615. <https://doi.org/10.1016/j.cell.2015.12.056>.
- Del-Aguila, J.L., Li, Z., Dube, U., Mihindukulasuriya, K.A., Budde, J.P., Fernandez, M.V., Ibanez, L., Bradley, J., Wang, F., Bergmann, K., et al. (2019). A single-nuclei RNA sequencing study of Mendelian and sporadic AD in the human brain. *Alzheimers Res. Ther.* 11, 71. <https://doi.org/10.1186/s13195-019-0524-x>.
- Diaz-Castro, B., Gangwani, M.R., Yu, X., Coppola, G., and Khakh, B.S. (2019). Astrocyte molecular signatures in Huntington's disease. *Sci. Transl. Med.* 11, eaaw8546.
- Dimas, P., Montani, L., Pereira, J.A., Moreno, D., Trötzmüller, M., Gerber, J., Semenkovich, C.F., Köfeler, H.C., and Suter, U. (2019). CNS myelination and remyelination depend on fatty acid synthesis by oligodendrocytes. *eLife* 8, e44702. <https://doi.org/10.7554/eLife.44702>.
- Durinck, S., Spellman, P.T., Birney, E., and Huber, W. (2009). Mapping identifiers for the integration of genomic datasets with the R/Bioconductor package biomaRt. *Nat. Protoc.* 4, 1184–1191. <https://doi.org/10.1038/nprot.2009.97>.
- Farkas, E., and Luiten, P.G.M. (2001). Cerebral microvascular pathology in aging and Alzheimer's disease. *Prog. Neurobiol.* 64, 575–611.
- Fünfschilling, U., Supplie, L.M., Mahad, D., Boretius, S., Saab, A.S., Edgar, J.J., Brinkmann, B.G., Kassmann, C.M., Tsvetanova, I.D., Möbius, W., et al. (2012). Glycolytic oligodendrocytes maintain myelin and long-term axonal integrity. *Nature* 485, 517–521. <https://doi.org/10.1038/nature11007>.
- Gerrits, E., Brouwer, N., Kooistra, S.M., Woodbury, M.E., Vermeiren, Y., Lambourne, M., Mulder, J., Kummer, M., Möller, T., Biber, K., et al. (2021). Distinct amyloid-beta and tau-associated microglia profiles in Alzheimer's disease. *Acta Neuropathol.* 141, 681–696. <https://doi.org/10.1007/s00401-021-02263-w>.
- Ginsberg, S.D., Che, S., Counts, S.E., and Mufson, E.J. (2006). Single cell gene expression profiling Alzheimer's disease. *NeuroRx* 3, 302–318.
- Goldberg, T.E., Huey, E.D., and Devanand, D.P. (2020). Association of APOE e2 genotype with Alzheimer's and non-Alzheimer's neurodegenerative pathologies. *Nat. Commun.* 11, 4727. <https://doi.org/10.1038/s41467-020-18198-x>.
- González-Reyes, R.E., Nava-Mesa, M.O., Vargas-Sánchez, K., Ariza-Salamanca, D., and Mora-Muñoz, L. (2017). Involvement of astrocytes in Alzheimer's disease from a neuroinflammatory and oxidative stress perspective. *Front. Mol. Neurosci.* 10, 427. <https://doi.org/10.3389/fnmol.2017.00427>.
- Grubman, A., Chew, G., Ouyang, J.F., Sun, G., Choo, X.Y., McLean, C., Simmons, R.K., Buckberry, S., Vargas-Landin, D.B., Poppe, D., et al. (2019). A single-cell atlas of entorhinal cortex from individuals with Alzheimer's disease reveals cell-type-specific gene expression regulation. *Nat. Neurosci.* 22, 2087–2097. <https://doi.org/10.1038/s41593-019-0539-4>.
- Gu, Z., Eils, R., and Schlesner, M. (2016). Complex heatmaps reveal patterns and correlations in multidimensional genomic data. *Bioinformatics* 32, 2847–2849. <https://doi.org/10.1093/bioinformatics/btw313>.
- Guttenplan, K.A., Weigel, M.K., Adler, D.I., Couthouis, J., Liddelow, S.A., Gitler, A.D., and Barres, B.A. (2020). Knockout of reactive astrocyte activating factors slows disease progression in an ALS mouse model. *Nat. Commun.* 11, 3753. <https://doi.org/10.1038/s41467-020-17514-9>.
- Guttenplan, K.A., Weigel, M.K., Prakash, P., Wijewardhane, P.R., Hasel, P., Rufen-Blanchette, U., Münch, A.E., Blum, J.A., Fine, J., Neal, M.C., et al. (2021). Neurotoxic reactive astrocytes induce cell death via saturated lipids. *Nature* 599, 102–107. <https://doi.org/10.1038/s41586-021-03960-y>.
- Hafemeister, C., and Satija, R. (2019). Normalization and variance stabilization of single-cell RNA-seq data using regularized negative binomial regression. *Genome Biol.* 20, 296. <https://doi.org/10.1186/s13059-019-1874-1>.
- Hao, Y., Hao, S., Andersen-Nissen, E., Mauck, W.M., 3rd, Zheng, S., Butler, A., Lee, M.J., Wilk, A.J., Darby, C., Zager, M., et al. (2021). Integrated analysis of multimodal single-cell data. *Cell* 184, 3573–3587.e29. <https://doi.org/10.1016/j.cell.2021.04.048>.
- Hasel, P., Rose, I.V.L., Sadick, J.S., Kim, R.D., and Liddelow, S.A. (2021). Neuroinflammatory astrocyte subtypes in the mouse brain. *Nat. Neurosci.* 24, 1475–1487. <https://doi.org/10.1038/s41593-021-00905-6>.
- Hattori, T., Shimizu, S., Koyama, Y., Yamada, K., Kuwahara, R., Kumamoto, N., Matsuzaki, S., Ito, A., Katayama, T., and Tohyama, M. (2010). DISC1 regulates N-cadherin and β 1-integrin expression in neurons. *Mol. Psychiatry* 15, 778. <https://doi.org/10.1038/mp.2010.83>.
- Hodge, R.D., Bakken, T.E., Miller, J.A., Smith, K.A., Barkan, E.R., Graybuck, L.T., Close, J.L., Long, B., Johansen, N., Penn, O., et al. (2019). Conserved cell types with divergent features in human versus mouse cortex. *Nature* 573, 61–68. <https://doi.org/10.1038/s41586-019-1506-7>.
- Hong, S., Beja-Glasser, V.F., Nfonoyim, B.M., Frouin, A., Li, S., Ramakrishnan, S., Merry, K.M., Shi, Q., Rosenthal, A., Barres, B.A., et al. (2016). Complement and microglia mediate early synapse loss in Alzheimer mouse models. *Science* 352, 712–716. <https://doi.org/10.1126/science.aad8373>.
- Huang, Z., Zhao, J., Wang, W., Zhou, J., and Zhang, J. (2020). Depletion of LncRNA NEAT1 rescues mitochondrial dysfunction through NEDD4L-dependent PINK1 degradation in animal models of Alzheimer's disease. *Front. Cell. Neurosci.* 14, 28. <https://doi.org/10.3389/fncel.2020.00028>.
- Jiang, H.Y., Wek, S.A., McGrath, B.C., Lu, D., Hai, T., Harding, H.P., Wang, X., Ron, D., Cavener, D.R., and Wek, R.C. (2004). Activating transcription factor 3 is integral to the eukaryotic initiation factor 2 kinase stress response. *Mol. Cell. Biol.* 24, 1365–1377. <https://doi.org/10.1128/MCB.24.3.1365-1377.2004>.
- Kay, M. (2021). ggdist: visualizations of distributions and uncertainty. <https://doi.org/10.5281/zenodo.3879620>.
- Kedmi, M., and Orr-Utreger, A. (2007). Expression changes in mouse brains following nicotine-induced seizures: the modulation of transcription factor networks. *Physiol. Genomics* 30, 242–252. <https://doi.org/10.1152/physiogenomics.00288.2006>.
- Kilinc, D. (2018). The emerging role of mechanics in synapse formation and plasticity. *Front. Cell. Neurosci.* 12, 483. <https://doi.org/10.3389/fncel.2018.00483>.
- Komarova, N.L., and Thalhauser, C.J. (2011). High degree of heterogeneity in Alzheimer's disease progression patterns. *PLoS Comput. Biol.* 7, e1002251. <https://doi.org/10.1371/journal.pcbi.1002251>.
- Korsunsky, I., Millard, N., Fan, J., Slowikowski, K., Zhang, F., Wei, K., Baglaenko, Y., Brenner, M., Loh, P.R., and Raychaudhuri, S. (2019). Fast, sensitive and accurate integration of single-cell data with harmony. *Nat. Methods* 16, 1289–1296. <https://doi.org/10.1038/s41592-019-0619-0>.
- Lau, S.F., Cao, H., Fu, A.K.Y., and Ip, N.Y. (2020). Single-nucleus transcriptome analysis reveals dysregulation of angiogenic endothelial cells and neuroprotective glia in Alzheimer's disease. *Proc. Natl. Acad. Sci. USA* 117, 25800–25809. <https://doi.org/10.1073/pnas.2008762117>.
- Lee, S., Viqar, F., Zimmerman, M.E., Narkhede, A., Tosto, G., Benzinger, T.L., Marcus, D.S., Fagan, A.M., Goate, A., Fox, N.C., et al. (2016). White matter hyperintensities are a core feature of Alzheimer's disease: evidence from the dominantly inherited Alzheimer network. *Ann. Neurol.* 79, 929–939. <https://doi.org/10.1002/ana.24647>.
- Leng, K., Li, E., Eser, R., Piergies, A., Sit, R., Tan, M., Neff, N., Li, S.H., Rodriguez, R.D., Suemoto, C.K., et al. (2021). Molecular characterization of selectively vulnerable neurons in Alzheimer's disease. *Nat. Neurosci.* 24, 276–287. <https://doi.org/10.1038/s41593-020-00764-7>.
- Lewandowski, N.M., Ju, S., Verbitsky, M., Ross, B., Geddie, M.L., Rockenstein, E., Adame, A., Muhammad, A., Vonsattel, J.P., Ringe, D., et al. (2010). Polyamine pathway contributes to the pathogenesis of Parkinson disease. *Proc. Natl. Acad. Sci. USA* 107, 16970–16975. <https://doi.org/10.1073/pnas.101751107>.
- Lian, H., Litvinchuk, A., Chiang, A.C., Aithmitti, N., Jankowsky, J.L., and Zheng, H. (2016). Astrocyte-microglia cross talk through complement activation modulates amyloid pathology in mouse models of Alzheimer's disease. *J. Neurosci.* 36, 577–589. <https://doi.org/10.1523/JNEUROSCI.2117-15.2016>.
- Liddelow, S.A., Guttenplan, K.A., Clarke, L.E., Bennett, F.C., Bohlen, C.J., Schirmer, L., Bennett, M.L., Münch, A.E., Chung, W.S., Peterson, T.C., et al. (2017). Neurotoxic reactive astrocytes are induced by activated microglia. *Nature* 541, 481–487. <https://doi.org/10.1038/nature21029>.

- Lie, E., Li, Y., Kim, R., and Kim, E. (2018). SALM/Lrfn family synaptic adhesion molecules. *Front. Mol. Neurosci.* 11, 105. <https://doi.org/10.3389/fnmol.2018.00105>.
- Lorente-Gea, L., García, B., Martín, C., Quirós, L.M., and Fernández-Vega, I. (2017). Heparan sulfate proteoglycans and heparanases in Alzheimer's disease: current outlook and potential therapeutic targets. *Neural Regen. Res.* 12, 914–915.
- Mathys, H., Davila-Velderrain, J., Peng, Z., Gao, F., Mohammadi, S., Young, J.Z., Menon, M., He, L., Abdurrob, F., Jiang, X., et al. (2019). Single-cell transcriptomic analysis of Alzheimer's disease. *Nature* 570, 332–337. <https://doi.org/10.1038/s41586-019-1195-2>.
- Mattsson, N., Schott, J.M., Hardy, J., Turner, M.R., and Zetterberg, H. (2016). Selective vulnerability in neurodegeneration: insights from clinical variants of Alzheimer's disease. *J. Neurol. Neurosurg. Psychiatry* 87, 1000–1004. <https://doi.org/10.1136/jnnp-2015-311321>.
- Maynard, K.R., Collado-Torres, L., Weber, L.M., Uytengco, C., Barry, B.K., Williams, S.R., Catallini, J.L., 2nd, Tran, M.N., Besich, Z., Tippani, M., et al. (2021). Transcriptome-scale spatial gene expression in the human dorsolateral prefrontal cortex. *Nat. Neurosci.* 24, 425–436. <https://doi.org/10.1038/s41593-020-00787-0>.
- Mohamed, L.A., Keller, J.N., and Kaddoumi, A. (2016). Role of P-glycoprotein in mediating rivastigmine effect on amyloid-beta brain load and related pathology in Alzheimer's disease mouse model. *Biochim. Biophys. Acta* 1862, 778–787. <https://doi.org/10.1016/j.bbadi.2016.01.013>.
- Murray, M.E., Graff-Radford, N.R., Ross, O.A., Petersen, R.C., Duara, R., and Dickson, D.W. (2011). Neuropathologically defined subtypes of Alzheimer's disease with distinct clinical characteristics: a retrospective study. *Lancet Neurol.* 10, 785–796. [https://doi.org/10.1016/S1474-4422\(11\)70156-9](https://doi.org/10.1016/S1474-4422(11)70156-9).
- Nedergaard, M., Ransom, B., and Goldman, S.A. (2003). New roles for astrocytes: redefining the functional architecture of the brain. *Trends Neurosci.* 26, 523–530. <https://doi.org/10.1016/j.tins.2003.08.008>.
- Nelson, P.T., Pious, N.M., Jicha, G.A., Wilcock, D.M., Fardo, D.W., Estus, S., and Rebeck, G.W. (2013). APOE-e2 and APOE-e4 correlate with increased amyloid accumulation in cerebral vasculature. *J. Neuropathol. Exp. Neurol.* 72, 708–715.
- Nott, A., Holtman, I.R., Coufal, N.G., Schlachetzki, J.C.M., Yu, M., Hu, R., Han, C.Z., Pena, M., Xiao, J., Wu, Y., et al. (2019). Brain cell type-specific enhancer-promoter interactome maps and disease-risk association. *Science* 366, 1134–1139.
- Nunes-Xavier, C.E., Zaldumbide, L., Arunetxeta, O., López-Almaraz, R., López, J.I., and Pulido, R. (2019). Dual-specificity phosphatases in neuroblastoma cell growth and differentiation. *Int. J. Mol. Sci.* 20, 1170. <https://doi.org/10.3390/ijms20051170>.
- O'Callaghan, P., Sandwall, E., Li, J.P., Yu, H., Ravid, R., Guan, Z.Z., van Kuppevelt, T.H., Nilsson, L.N., Ingelsson, M., Hyman, B.T., et al. (2008). Heparan sulfate accumulation with Abeta deposits in Alzheimer's disease and Tg2576 mice is contributed by glial cells. *Brain Pathol.* 18, 548–561. <https://doi.org/10.1111/j.1750-3639.2008.00152.x>.
- Owen, J.B., Di Domenico, F., Sultana, R., Perlutigi, M., Cini, C., Pierce, W.M., and Butterfield, D.A. (2009). Proteomics-determined differences in the concanavalin-A-fractionated proteome of hippocampus and inferior parietal lobule in subjects with Alzheimer's disease and mild cognitive impairment: implications for progression of AD. *J. Proteome Res.* 8, 471–482. <https://doi.org/10.1021/pr800667a>.
- Pardo, B., Spangler, A., Weber, L.M., Hicks, S.C., Jaffe, A.E., Martinowich, K., Maynard, K.R., and Collado-Torres, L. (2021). spatialLIBD: an R/Bioconductor package to visualize spatially-resolved transcriptomics data. Preprint at bioRxiv. 2021.2004.2029.440149. <https://doi.org/10.1101/2021.04.29.440149>.
- Paton, C.M., and Ntambi, J.M. (2009). Biochemical and physiological function of stearoyl-CoA desaturase. *Am. J. Physiol. Endocrinol. Metab.* 297, E28–E37. <https://doi.org/10.1152/ajpendo.90897.2008>.
- Prickaerts, J., Heckman, P.R.A., and Blokland, A. (2017). Investigational phosphodiesterase inhibitors in phase I and phase II clinical trials for Alzheimer's disease. *Expert Opin. Investig. Drugs* 26, 1033–1048. <https://doi.org/10.1080/13543784.2017.1364360>.
- Radanovic, M., Ramos, F., Pereira, S., Stella, F., Aprahamian, I., Ferreira, L.K., Forlenza, O.V., and Busatto, G.F. (2013). White matter abnormalities associated with Alzheimer's disease and mild cognitive impairment: a critical review of MRI studies. *Expert Rev. Neurotherapeutics* 13, 483–493.
- Ramsay, L., Quillé, M.L., Orset, C., de la Grange, P., Rousselet, E., Férec, C., Le Gac, G., Génin, E., and Timsit, S. (2019). Blood transcriptomic biomarker as a surrogate of ischemic brain gene expression. *Ann. Clin. Transl. Neurol.* 6, 1681–1695. <https://doi.org/10.1002/acn3.50861>.
- Refolo, L.M., Malester, B., LaFrancois, J., Bryant-Thomas, T., Wang, R., Tint, G.S., Sambamurti, K., Duff, K., and Pappolla, M.A. (2000). Hypercholesterolemia accelerates the Alzheimer's amyloid pathology in a transgenic mouse model. *Neurobiol. Dis.* 7, 321–331. <https://doi.org/10.1006/nbdi.2000.0304>.
- Reiman, E.M., Arboleda-Velasquez, J.F., Quiroz, Y.T., Huentelman, M.J., Beach, T.G., Caselli, R.J., Chen, Y., Su, Y., Myers, A.J., Hardy, J., et al. (2020). Exceptionally low likelihood of Alzheimer's dementia in APOE2 homozygotes from a 5,000-person neuropathological study. *Nat. Commun.* 11, 667. <https://doi.org/10.1038/s41467-019-14279-8>.
- Risso, D., Perraudeau, F., Gribkova, S., Dudoit, S., and Vert, J.P. (2018). A general and flexible method for signal extraction from single-cell RNA-seq data. *Nat. Commun.* 9, 284. <https://doi.org/10.1038/s41467-017-02554-5>.
- Robinson, M.D., McCarthy, D.J., and Smyth, G.K. (2010). edgeR: a Bioconductor package for differential expression analysis of digital gene expression data. *Bioinformatics* 26, 139–140. <https://doi.org/10.1093/bioinformatics/btp616>.
- Saab, A.S., Tzvetavona, I.D., Trevisoli, A., Baltan, S., Dibaj, P., Kusch, K., Möbius, W., Goetze, B., Jahn, H.M., Huang, W., et al. (2016). Oligodendroglial NMDA receptors regulate glucose import and axonal energy metabolism. *Neuron* 91, 119–132. <https://doi.org/10.1016/j.neuron.2016.05.016>.
- Sadick, J.S., and Liddelow, S.A. (2019). Don't forget astrocytes when targeting Alzheimer's disease. *Br. J. Pharmacol.* 176, 3585–3598. <https://doi.org/10.1111/bph.14568>.
- Saher, G., Brügger, B., Lappe-Siefke, C., Möbius, W., Tozawa, R., Wehr, M.C., Wieland, F., Ishibashi, S., and Nave, K.A. (2005). High cholesterol level is essential for myelin membrane growth. *Nat. Neurosci.* 8, 468–475. <https://doi.org/10.1038/nn1426>.
- Saher, G., Quintes, S., and Nave, K.A. (2011). Cholesterol: a novel regulatory role in myelin formation. *Neuroscientist* 17, 79–93. <https://doi.org/10.1177/1073858410373835>.
- Schindelin, J., Arganda-Carreras, I., Frise, E., Kaynig, V., Longair, M., Pietzsch, T., Preibisch, S., Rueden, C., Saalfeld, S., Schmid, B., et al. (2012). Fiji: an open-source platform for biological-image analysis. *Nat. Methods* 9, 676–682. <https://doi.org/10.1038/nmeth.2019>.
- Schipper, H.M., Bennett, D.A., Liberman, A., Bienias, J.L., Schneider, J.A., Kelly, J., and Arvanitakis, Z. (2006). Glial heme oxygenase-1 expression in Alzheimer disease and mild cognitive impairment. *Neurobiol. Aging* 27, 252–261. <https://doi.org/10.1016/j.neurobiolaging.2005.01.016>.
- Schnädelbach, O., Ozen, I., Blaschuk, O.W., Meyer, R.L., and Fawcett, J.W. (2001). N-cadherin is involved in axon-oligodendrocyte contact and myelination. *Mol. Cell. Neurosci.* 17, 1084–1093. <https://doi.org/10.1006/mcne.2001.0961>.
- Shepardson, N.E., Shankar, G.M., and Selkoe, D.J. (2011). Cholesterol level and statin use in Alzheimer disease: I. Review of epidemiological and preclinical studies. *Arch. Neurol.* 68, 1239–1244. <https://doi.org/10.1001/archneurol.2011.203>.
- Shi, Y., Yamada, K., Liddelow, S.A., Smith, S.T., Zhao, L., Luo, W., Tsai, R.M., Spina, S., Grinberg, L.T., Rojas, J.C., et al. (2017). ApoE4 markedly exacerbates tau-mediated neurodegeneration in a mouse model of tauopathy. *Nature* 549, 523–527. <https://doi.org/10.1038/nature24016>.

- Smith, H.L., Freeman, O.J., Butcher, A.J., Holmqvist, S., Humoud, I., Schätzl, T., Hughes, D.T., Verity, N.C., Swinden, D.P., Hayes, J., et al. (2020). Astrocyte unfolded protein response induces a specific reactivity state that causes non-cell-autonomous neuronal degeneration. *Neuron* 105, 855–866.e5. <https://doi.org/10.1016/j.neuron.2019.12.014>.
- Stogsdill, J.A., Ramirez, J., Liu, D., Kim, Y.H., Baldwin, K.T., Enustun, E., Ejikeme, T., Ji, R.R., and Ergo, C. (2017). Astrocytic neuroligins control astrocyte morphogenesis and synaptogenesis. *Nature* 551, 192–197. <https://doi.org/10.1038/nature24638>.
- Stuart, T., Butler, A., Hoffman, P., Hafemeister, C., Papalexi, E., Mauck, W.M., 3rd, Hao, Y., Stoeckius, M., Smibert, P., and Satija, R. (2019). Comprehensive integration of single-cell data. *Cell* 177, 1888–1902.e21. <https://doi.org/10.1016/j.cell.2019.05.031>.
- Syed, Y.A., Baer, A., Hofer, M.P., González, G.A., Rundle, J., Myrta, S., Huang, J.K., Zhao, C., Rossner, M.J., Trotter, M.W., et al. (2013). Inhibition of phosphodiesterase-4 promotes oligodendrocyte precursor cell differentiation and enhances CNS remyelination. *EMBO Mol. Med.* 5, 1918–1934. <https://doi.org/10.1002/emmm.201303123>.
- Taylor, D.M., Moser, R., Régulier, E., Breuillaud, L., Dixon, M., Beesen, A.A., Elliston, L., Silva Santos, Mde F., Kim, J., Jones, L., et al. (2013). MAP kinase phosphatase 1 (MKP-1/DUSP1) is neuroprotective in Huntington's disease via additive effects of JNK and p38 inhibition. *J. Neurosci.* 33, 2313–2325. <https://doi.org/10.1523/JNEUROSCI.4965-11.2013>.
- Teakton, T., Graham, A., Court, J., Perry, R., Jaros, E., Johnson, M., Hall, R., and Perry, E. (2003). Alzheimer's disease is associated with a selective increase in alpha7 nicotinic acetylcholine receptor immunoreactivity in astrocytes. *Glia* 41, 207–211. <https://doi.org/10.1002/glia.10132>.
- Tirosh, I., Izar, B., Prakadan, S.M., Wadsworth, M.H., 2nd, Treacy, D., Trombetta, J.J., Rotem, A., Rodman, C., Lian, C., Murphy, G., et al. (2016). Dissecting the multicellular ecosystem of metastatic melanoma by single-cell RNA-seq. *Science* 352, 189–196. <https://doi.org/10.1126/science.aad0501>.
- Vidal, R., Frangione, B., Rostagno, A., Mead, S., Révész, T., Plant, G., and Ghiso, J. (1999). A stop-codon mutation in the BRI gene associated with familial British dementia. *Nature* 399, 776–781.
- Viswanathan, A., and Greenberg, S.M. (2011). Cerebral amyloid angiopathy in the elderly. *Ann. Neurol.* 70, 871–880. <https://doi.org/10.1002/ana.22516>.
- von Bartheld, C.S., Bahney, J., and Herculano-Houzel, S. (2016). The search for true numbers of neurons and glial cells in the human brain: a review of 150 years of cell counting. *J. Comp. Neurol.* 524, 3865–3895. <https://doi.org/10.1002/cne.24040>.
- Wu, T., Dejanovic, B., Gandham, V.D., Gogineni, A., Edmonds, R., Schauer, S., Srinivasan, K., Huntley, M.A., Wang, Y., Wang, T.M., et al. (2019). Complement C3 is activated in human AD brain and is required for neurodegeneration in mouse models of amyloidosis and tauopathy. *Cell Rep.* 28, 2111–2123.e6. <https://doi.org/10.1016/j.celrep.2019.07.060>.
- Wu, Y., Li, Z., Huang, Y.Y., Wu, D., and Luo, H.B. (2018). Novel phosphodiesterase inhibitors for cognitive improvement in Alzheimer's disease. *J. Med. Chem.* 61, 5467–5483. <https://doi.org/10.1021/acs.jmedchem.7b01370>.
- Wu, Z., Zhao, L., Chen, X., Cheng, X., and Zhang, Y. (2015). Galantamine attenuates amyloid-beta deposition and astrocyte activation in APP/PS1 transgenic mice. *Exp. Gerontol.* 72, 244–250. <https://doi.org/10.1016/j.exger.2015.10.015>.
- Yip, C.M., Elton, E.A., Darabie, A.A., Morrison, M.R., and McLaurin, J. (2001). Cholesterol, a modulator of membrane-associated Abeta-fibrillogenesis and neurotoxicity. *J. Mol. Biol.* 311, 723–734. <https://doi.org/10.1006/jmbi.2001.4881>.
- Yue, C., and Jing, N. (2015). The promise of stem cells in the therapy of Alzheimer's disease. *Transl. Neurodegener.* 4, 8. <https://doi.org/10.1186/s40035-015-0029-x>.
- Zamanian, J.L., Xu, L., Foo, L.C., Nouri, N., Zhou, L., Giffard, R.G., and Barres, B.A. (2012). Genomic analysis of reactive astrogliosis. *J. Neurosci.* 32, 6391–6410. <https://doi.org/10.1523/JNEUROSCI.6221-11.2012>.
- Zhang, Y., Sloan, S.A., Clarke, L.E., Caneda, C., Plaza, C.A., Blumenthal, P.D., Vogel, H., Steinberg, G.K., Edwards, M.S., Li, G., et al. (2016). Purification and characterization of progenitor and mature human astrocytes reveals transcriptional and functional differences with mouse. *Neuron* 89, 37–53. <https://doi.org/10.1016/j.neuron.2015.11.013>.
- Zhang, Z.G., Zhang, L., Jiang, Q., Zhang, R., Davies, K., Powers, C., van Bruggen, Nv, and Chopp, M. (2000). VEGF enhances angiogenesis and promotes blood-brain barrier leakage in the ischemic brain. *J. Clin. Invest.* 106, 829–838.
- Zhao, E., Stone, M., Ren, X., et al.; Raphael Gottardo (2021). Spatial transcriptomics at subspot resolution with BayesSpace. *Nat. Biotechnol.* 39, 1375–1384. <https://doi.org/10.1038/s41587-021-00935-2>.
- Zhong, L., Xie, Y.Z., Cao, T.T., Wang, Z., Wang, T., Li, X., Shen, R.C., Xu, H., Bu, G., and Chen, X.F. (2016). A rapid and cost-effective method for genotyping apolipoprotein E gene polymorphism. *Mol. Neurodegener.* 11, 2. <https://doi.org/10.1186/s13024-016-0069-4>.
- Zhou, Y., Song, W.M., Andhey, P.S., Swain, A., Levy, T., Miller, K.R., Poliani, P.L., Cominelli, M., Grover, S., Gilfillan, S., et al. (2020). Human and mouse single-nucleus transcriptomics reveal TREM2-dependent and TREM2-independent cellular responses in Alzheimer's disease. *Nat. Med.* 26, 131–142. <https://doi.org/10.1038/s41591-019-0695-9>.

STAR★METHODS

KEY RESOURCE TABLE

REAGENT or RESOURCE	Source	Identifier
Antibodies		
Mouse Anti-Amyloid-Beta 17–24	BioLegends	Cat#800701; RRID:AB_2564633
Mouse Anti-Phospho-Tau, Ser202/Thr205 Monoclonal	Thermo Fisher Scientific	Cat#MN1020; RRID:AB_223647
Rabbit Anti-Glial Fibrillary Acidic Protein (EP672Y)	Ventana	Cat#760-4345
Discovery Universal Secondary Biotinylated Antibody Cocktail	Roche	Cat#760-4205; RRID:AB_10805231
Rabbit Anti-SOX9 (EPR14335-78)	Abcam	Cat#ab185966; RRID:AB_2728660
Rabbit IgG Isotype Control (EPR25A)	Abcam	Cat#ab172730; RRID:AB_2687931
Mouse Anti-Human SPARC (Clone: 122511)	R&D Systems (Minneapolis, United States of America)	Cat# MAB941, RRID:AB_2195073
Mouse Anti-GFAP	Sigma-Aldrich	Cat# G3893, RRID:AB_477010
Rabbit Anti-GFAP	DAKO	Cat# Z0034
Rabbit Anti-Human C3d	DAKO	Cat# A0063
Goat Anti-Rabbit IgG (H+L) Cross-Adsorbed ReadyProbes Secondary Antibody, Alexa Fluor 594	Thermo Fisher Scientific	Cat#R37117; RRID:AB_2556545
Rabbit Anti-LIM Homeobox 2 LHX2	EMD Millipore	Cat#AB5756; RRID:AB_92012
Mouse Anti-NeuN (Clone A60)	Millipore Sigma	Cat#MAB377; RRID:AB_2298772
Mouse IgG1 Isotype Control (Clone Ci4)	Millipore Sigma	Cat#MABC002; RRID:AB_97846
Goat Anti-Rabbit IgG (H+L) Highly Cross-Adsorbed Secondary Antibody, Alexa Fluor 488	Invitrogen (Paisley, UK)	Cat#A11034; RRID:AB_2576217
Goat Anti-Rabbit IgG (H+L) Highly Cross-Adsorbed Secondary Antibody, Alexa Fluor 594	Invitrogen	Cat# A11012, RRID:AB_2534079
Goat Anti-Mouse IgG (H+L) Cross-Adsorbed Secondary Antibody, Alexa Fluor 647	Invitrogen	Cat#A21235; RRID:AB_2535804
Biological Samples		
De-Identified Human, Post-Mortem Prefrontal Cortex Samples from Alzheimer's Disease and Age-Matched Non-Symptomatic Patients	Rhode Island Hospital's Brain Tissue Resource Center Table S2	https://www.brown.edu/research/facilities/brain-tissue-resource-center/
De-Identified Human, Post-Mortem Prefrontal Cortex Samples from Alzheimer's Disease and Age-Matched Non-Symptomatic Patients	Alzheimer's disease Research Center at NYU Langone Table S2	https://med.nyu.edu/departments-institutes/neurology/divisions-centers/center-cognitive-neurology/alzheimers-disease-center
De-Identified Human, Post-Mortem Prefrontal Cortex Samples from Alzheimer's Disease and Age-Matched Non-Symptomatic Patients	Shiley-Marcos Alzheimer's disease Research Center at UCSD Table S2	https://medschool.ucsd.edu/som/neurosciences/centers/adrc/Pages/default.aspx
Chemicals, Peptides, and Recombinant Proteins		
Rnase-Free Buffer Kit	Invitrogen	Cat#Am9010
Triton X100	Sigma	Cat#T8787
Rnasin Plus	Promega (Southampton, UK)	Cat#N2615
Protease Inhibitor Cocktail	Promega	Cat#G6521

(Continued on next page)

Continued

REAGENT or RESOURCE	Source	Identifier
DL-Dithiothreitol	Sigma	Cat#D9779
Dnase- and Rnase-Free Water	Invitrogen	Cat#10977015
Reagent-Grade Bovine Serum Albumin	Proliant Biologicals	Cat#68700
Goat Serum	MP Biomedicals (Irvine, CA, United States of America)	Cat#191356
4',6 Diamidino 2 Phenylindole, Dihydrochloride	Thermo Fisher Scientific	Cat#D1306
Phosphate Buffer Saline	VWR	Cat#16750-102
Critical Commercial Assays		
QIAshredder	QIAGEN	Cat#79656
Rneasy Plus Mini Kits	QIAGEN	Cat#74136
GoTaq Green Master Mix	Promega	Cat#M7123
Single Cell 3' Gene Expression Kit v3	10x Chromium	Cat#1000076
Deposited Data		
Pathology Imaging Data	This paper	Cell Image Library: http://cellimagelibrary.org/groups/54423
Single Nuclei RNA Sequencing Data (FASTQ and Cell Ranger-Generated Matrix Files)	This paper	GEO: GSE167494; https://www.ncbi.nlm.nih.gov/geo/query/acc.cgi?acc=GSE167494
Single Nuclei RNA Sequencing Data (FASTQ Files)	Mathys et al. (2019)	Synapse: syn18485175; https://www.synapse.org/#!Synapse:syn18485175
Single Nuclei RNA Sequencing Data (FASTQ Files)	Grubman et al. (2019)	GEO: GSE138852; https://www.ncbi.nlm.nih.gov/geo/query/acc.cgi?acc=GSE138852
Single Nuclei RNA Sequencing Data (FASTQ Files)	Zhou et al. (2020)	Synapse: syn21670836; https://www.synapse.org/#!Synapse:syn21670836
Oligonucleotides		
APOE_e2_FWD: 5'-GCGGACATGGAG GACGTGT-3'	Zhong et al. (2016)	N/A
APOE_e2_REV: 5'-CCTGGTACACTGC CAGGCA-3'	Zhong et al. (2016)	N/A
APOE_e3_FWD: 5'-CGGACATGGAGG ACGTGT-3'	Zhong et al. (2016)	N/A
APOE_e3_REV: 5'-CTGGTACACTGCC AGGCG-3'	Zhong et al. (2016)	N/A
APOE_e4_FWD: 5'-CGGACATGGAGG ACGTGC-3'	Zhong et al. (2016)	N/A
APOE_e4_REV: 5'-CTGGTACACTGCC AGGCG-3'	Zhong et al. (2016)	N/A
B-actin_FWD: 5'-GACGTGGACATCCG CAAAGAC-3'	Zhong et al. (2016)	N/A
B-actin_REV: 5'-CAGGTCAGCTCAGG CAGGAA-3'	Zhong et al. (2016)	N/A
Software and Algorithms		
QuPath (version 0.2.3)	Bankhead et al. (2017)	https://qupath.github.io/ ; RRID:SCR_018257
Fiji-ImageJ (version 2.1.0)	Schindelin et al. (2012)	https://imagej.net/Fiji ; RRID:SCR_003070
Prism (version 9.0.0)	GraphPad	https://www.graphpad.com/scientific-software/prism/ ; RRID:SCR_002798

(Continued on next page)

Continued

REAGENT or RESOURCE	Source	Identifier
FlowJo (version 10.7.1)	BD	https://www.flowjo.com/ ; RRID:SCR_008520
NovaSeq 6000 RTA (version 3.4.4)	Illumina	https://support.illumina.com/sequencing/sequencing_instruments/novaseq-6000.html ; RRID:SCR_014332
bcl2fastq Conversion Software (version 2.20)	Illumina	https://support.illumina.com/downloads/bcl2fastq-conversion-software-v2-20.html ; RRID:SCR_015058
Cell Ranger Software Suite (version 4.0.0)	10x Genomics	https://support.10xgenomics.com/single-cell-gene-expression/software/pipelines/latest/installation ; RRID:SCR_017344
R (Versions 3.6.2–4.1.1)	The R Foundation	https://www.r-project.org/foundation/ ; RRID:SCR_001905
<i>SingleCellExperiment</i> (version 1.12.0)	Amezquita et al. (2020)	https://bioconductor.org/packages/release/bioc/html/SingleCellExperiment.html
Seurat (version 3.2.2)	Stuart et al. (2019)	https://satijalab.org/seurat/index.html ; RRID:SCR_016341
Zinbwave (version 1.12.0)	Risso et al. (2018)	https://bioconductor.org/packages/release/bioc/html/zinbwave.html
edgeR (version 3.32.0)	Robinson et al. (2010)	https://bioconductor.org/packages/release/bioc/html/edgeR.html ; RRID:SCR_012802
All Rscripts Used to Analyze Single Nuclei RNA Sequencing Data	This paper	https://github.com/liddelowlab/Sadick_et_al_2022
Other		
Open-Access, Interactive Website Highlighting All Analyzed Single Nuclei RNA Sequencing Data	This paper	www.gliaseq.com

RESOURCE AVAILABILITY

Lead contact

For further information and resource/reagent requests, please direct all inquiries to the [Lead Contact](#), Shane Liddelow (shane.liddelow@nyulangone.org).

Materials availability

This study did not generate any unique reagents.

Data and code availability

- Raw snRNA-seq data generated in this study (including both FASTQ and Cell Ranger-generated matrix files) are available at GEO (GSE167494). Microscopy data reported in this paper are available through the Cell Image Library (www.cellimagelibrary.org, CIL group#: 54423).
- All code for analysis of original and previously published snRNA-seq, scRNA-seq, and spatial transcriptomic datasets are available on the Liddelow Lab GitHub page: https://github.com/liddelowlab/Sadick_et_al_2022.
- Analyzed snRNA-seq and pseudobulk snRNA-seq data is available on an open-access, interactive website: www.gliaseq.com. Any additional information required to reanalyze the data reported in this paper is available from the [lead contact](#) upon request.

EXPERIMENTAL MODEL AND SUBJECT DETAILS

Postmortem human cohorts

Pilot cohort

Five de-identified human donor prefrontal cortex samples (NS patients, N = 3; AD patients, N = 2) were provided by Rhode Island Hospital's Brain Tissue Resource Center (Title 45 CRF Part 46.102(f)) and New York University's AD Research Center (ADRC). All

tissues were donated with pre-mortem informed consent as regulated by Institute Review Boards at each respective Institution. In total, this donor cohort was comprised of one female and four male donors with ages ranging between 60 and 90 years of age and APOE genotypes of ϵ 2/3, ϵ 3/3, and ϵ 3/4. Post-mortem intervals ranged between 12 and 24 h for all tissues.

Final cohort

Sixteen de-identified human donor prefrontal cortex samples (NS patients, N = 6; AD patients, N = 10; with an additional N = 6 NS and AD patient samples for immunostaining validation studies) were provided by NYU Grossman School of Medicine's Alzheimer's Disease Research Center and University of California San Diego Shiley-Marcos ADRC. All tissues were donated with pre-mortem informed consent as regulated by Institute Review Boards at each respective Institution. In total, this donor cohort was comprised of 7 female and 9 male donors with ages ranging between 56 and 100 years of age. All donors had APOE genotypes of ϵ 2/3. Post-mortem intervals ranged between 5 and 100 h across all tissues. All samples had RNA Integrity Number (RIN) scores greater than 8. Based on sequencing analysis, two donors (Donors 5 and 9) were removed from final analyses, resulting in a total of 5 NS and 9 AD patients. Additional donor information is listed in [Table S2](#) (any patient-specific information that is not included in these de-identified tables can be obtained from the original brain bank – donor IDs provided for coordination).

METHOD DETAILS

Tissue RNA quality verification

In order to ensure high quality outputs from snRNA-seq experiments, all donor tissue samples were first evaluated for bulk RNA quality, as quantified by RIN scores. Bulk RNA was extracted from each donor (~15–30 mg of postmortem frozen human prefrontal cortex tissue) using QIAshredder (Qiagen, 79656) and Rneasy Plus Mini kits (Qiagen, 74136), following manufacturer's instructions. In brief, after each tissue was homogenized in lysis buffer using a Wheaton Dounce tissue grinder (DWK Life Sciences, 357538), samples were transferred to QIAshredder columns, flowthroughs were processed using Rneasy spin columns, and RNA from each sample was eluted in 30 μ L Dnase- and Rnase-free water (Invitrogen, 10977015). RIN scores were then generated using an Agilent (Santa Clara, CA, United States of America) 2100 Bioanalyzer ([Table S2](#)).

APOE genotype verification

To confirm APOE genotype identification provided by NYU and UCSD ADRCs, all final human cohort samples were validated in-house by PCR using single nucleotide polymorphism-specific primers for each allele (i.e., ϵ 2, ϵ 3, ϵ 4) and loading positive control β -actin, as designed by Zhong and colleagues ([Zhong et al., 2016](#)). The HotSHOT method was followed to isolate genomic DNA (gDNA). In brief, 10–30 mg of postmortem frozen human prefrontal cortex tissue per sample was digested in 75 μ L of alkaline lysis reagent (25 mM NaOH, 0.2 mM EDTA in Dnase- and Rnase-free water) at 98°C in a thermomixer for 1 h. To stop the reaction, 75 μ L of neutralizing reagent (40 mM Tris-HCl, pH 5.5 in Dnase- and Rnase-free water) was added to each sample, and the solution was centrifuged at 4,000 rpm for 3 min. The supernatant, now containing gDNA, was then used in all following PCR reactions. Twenty-five microliters PCR reactions were prepared for each sample and primer combination using GoTaq Green Master Mix (Promega, M7123) and respective primers (working dilution of 0.25 μ M), following manufacturer's instructions. PCR products were then run on 1.5% agarose gels (Thermo Fisher Scientific, 16-500-100) with ethidium bromide (VWR, 470024-556) for 40 min and were imaged using a Bio-Rad (Hercules, CA, United States of America) Gel Doc system ([Figure S1D](#)).

Immunohistochemistry and imaging of postmortem frozen human prefrontal cortex tissue

To evaluate pathological load in the final donor cohort, ~100 mg of postmortem frozen human prefrontal cortex tissue per donor was sent to the Neuropathology Brain Bank and Research CoRE at the Icahn School of Medicine at Mount Sinai for tissue fixation/embedding, sectioning, and staining. In brief, flash frozen tissues were fixed in 10% neutral buffered formalin and were then embedded in paraffin. Five- μ m sections were cut of each sample block for subsequent immunohistochemistry (IHC) assessments (N = 2–5 sections per stain). Primary antibodies used for IHC stains included: anti-amyloid- β (4G8) (BioLegends, 800701, 1:8000), anti-phosphorylated tau (AT8) (Thermo Fisher Scientific, MN1020, Ser202/Thr205 monoclonal, 1:1000), and anti-GFAP (Ventana, 760-4345, 1:10). Primary antibodies were detected using DISCOVERY universal secondary biotinylated antibody cocktail (Roche, 760-4205). Roche ultraView reagents were used in the preparation of all IHCs, and IHC stains were performed on a Ventana Benchmark XT following manufacturer's instructions. All IHC slides were counterstained with hematoxylin prior to visualization. In addition to IHC stains, donor samples were prepared with a modified Bielschowksy's silver stain in order to visualize diffuse plaques, neuritic plaques, and neurofibrillary tangles. Slides were scanned using a Leica (Wetzlar, Germany) SCN400 F whole-slide scanner through NYU Langone's Experimental Pathology Core. All slides were blinded for imaging and subsequent evaluation/quantification using QuPath (v0.2.3) software ([Bankhead et al., 2017](#)). Raw images are available through the Cell Image Library (CIL group#: 54423).

Quantification of 4G8 and AT8 IHC

For 4G8 and AT8 quantification, hematoxylin and DAB stains were separated using the default H-DAB color deconvolution settings for downstream quantifications. To quantify the area of each tissue section, the region of the section was defined using a custom pixel classifier, classifying pixels at a resolution of 2 μ m, with a hematoxylin channel threshold of 0.01 after applying a gaussian filter (σ = 2). To quantify amyloid- β plaques, 4G8 staining within each section's region of interest (ROI) was quantified using a second custom pixel classifier, which classified pixels at a resolution of 0.25 μ m, with a DAB stain value greater than 0.2 as 4G8-positive and

excluded any positive signal that was $< 5 \mu\text{m}^2$ in area. To quantify neurofibrillary tangles, AT8 staining within each section's ROI was quantified using a second custom pixel classifier, which classified pixels at a resolution of $0.25 \mu\text{m}$, with a DAB stain value greater than 0.5 as AT8-positive. Additionally, to count AT8⁺ cell bodies, the same custom pixel classifier was applied with an additional parameter to remove any AT8⁺ signal that was smaller than $60 \mu\text{m}^2$ or larger than $1200 \mu\text{m}^2$ (completed post-hoc in R). For both 4G8 and AT8 staining, normalized pixel density (4G8 or AT8 staining/total tissue area) was calculated in R (v4.0.3), and total counts and areas of each feature (i.e., 4G8⁺ plaques and AT8⁺ cell bodies) were also tallied. All raw quantifications for 4G8 and AT8 are provided in [Table S2](#).

Quantification of GFAP IHC

For GFAP quantification, hematoxylin and DAB stains were first separated using the default H-DAB color deconvolution settings to separate stains for downstream quantification. To quantify the area of each tissue section, the region of the section was defined using a custom pixel classifier, classifying pixels at a resolution of $2 \mu\text{m}$, with a value greater than or equal to 215 after applying a gaussian filter ($\sigma = 1.5$). Continuous regions of pixels exceeding the threshold were classified as belonging to the tissue section, after excluding small regions less than $10,000 \mu\text{m}^2$ in area which were detached from the majority of the section. Densely stained regions of artifact on the edges of the sections, if present, were manually selected using the brush tool and excluded from the final ROI defining the section. Next, the total area of GFAP staining within each section was quantified. The area of GFAP staining within each section's ROI was then quantified using a second custom pixel classifier, which classified pixels at a resolution of $0.25 \mu\text{m}$, with a DAB stain value greater than 0.25 as GFAP-positive. To normalize across sections of different areas, GFAP staining was reported as the proportion of the pixels in the section's ROI that were GFAP⁺. The average proportion of pixels that were GFAP⁺ for the sections from each donor was then calculated using R.

In addition to normalized pixel density, the average area of the astrocytes in each section was quantified using QuPath, Fiji ([Schindelin et al., 2012](#)), and R. First, quantifiable astrocytes in each section were identified manually as GFAP⁺ cells with an identifiable cell body and several processes that could be distinguished from the processes of adjacent astrocytes. All quantifiable astrocytes from a given section were numbered, and a maximum of 8 astrocytes from each section were randomly selected for quantification using R. In sections from two (out of 16) donors (specifically D2 and D6), no quantifiable astrocytes could be identified, and thus these donors were excluded from further analysis. Each randomly chosen astrocyte was then analyzed using Fiji. ROIs were manually drawn around each astrocyte using the freehand tool such that the GFAP staining contained within each ROI appeared to correspond to only the chosen astrocyte. The region outside the ROI was then excluded, and the included astrocyte was then segmented via manual thresholding using the default method. Then, the area of the segmented astrocyte was measured. The average area of the astrocytes from each donor was then calculated using R. All raw quantifications for GFAP are provided in [Table S2](#).

Semi-quantification of Bielschowsky's silver stain

At $15\times$ magnification, 5 ROIs were drawn randomly in each tissue section for manual assessment. Diffuse plaques, neuritic plaques, and neurofibrillary tangles were manually counted in each ROI. Based on total pathology feature counts, samples were given broad descriptors indicating none, low, moderate, or severe pathology. Raw pathological feature counts and overall descriptors are listed in [Table S2](#).

Validation of transcriptomic DEGs using antibody staining

Formalin-Fixed Paraffin-Embedded (FFPE) human brain tissue was sectioned to $5 \mu\text{m}$ and mounted on microscope slides. The sections were dewaxed at 60°C for 30 min and then transferred into HistoChoice (Sigma) for 2 washes for 5 min each. Sections were then moved into 100%, 95% and 70% ethanol for rehydration followed by three washes in PBS. For C3 staining, sections underwent antigen retrieval in M6 buffer (2.1% citric acid monohydrate, 2.94% tri-sodium citrate in dH_2O , pH 6) at 95°C for 10 min.

Sections were then blocked in blocking buffer containing 10% normal goat serum (NGS), 0.4% Triton X-100 (Sigma) in PBS for 1h at room temperature. The following primary antibodies were used: C3d (Dako A0063, rabbit 1:600), GFAP (Dako Z0034, rabbit, 1:500), GFAP (Sigma G3893, mouse, 1:400) and SPARC (R&D MAB941, mouse, 25 $\mu\text{g/mL}$). Sections were incubated in the primary antibodies over night at 4°C in blocking buffer followed by three washes in PBS. Sections were then incubated in the following secondary antibodies: goat anti-rabbit Alexa 594 (Invitrogen) and goat anti-mouse Alexa 488 (Abcam) at room temperature for 1h. Sections were then washed in PBS, incubated in TrueBlack (Biotium, Hayward, CA, United States of America) for 1 min, counter-stained with DAPI and mounted using Fluoromount-G (Southern Biotech). All images were acquired on a Keyence BZ-X710 using a $20\times$ objective and processed in Fiji.

Isolation of nuclei from postmortem frozen human prefrontal cortex tissue

The protocol followed to isolate nuclei from postmortem frozen human brain tissue was based off of a previously published study ([Hodge et al., 2019](#)). Processing of tissue was completed on ice or at 4°C for the entirety of the protocol. In brief, ~ 100 mg of postmortem frozen human prefrontal cortex per donor was homogenized in 2 mL homogenization buffer (10 mM Tris pH 8 (Invitrogen, Am9010), 250 mM sucrose (Invitrogen, Am9010), 25 mM KCl (Invitrogen, Am9010), 5 mM MgCl₂ (Invitrogen, Am9010), 0.1% Triton X100 (Sigma, T8787), 1% Rnasin Plus (Promega, N2615), 1× protease inhibitor (Promega, G6521), and 0.1 mM DTT (Sigma, D9779) in DNase- and RNase-free water) using a Wheaton Dounce tissue grinder (10 strokes with loose pestle, followed by 10 strokes with the tight pestle). Then, the homogenized tissue was filtered through 30 μm pre-separation filters (Miltenyi, 130-041-407) to remove major debris. Samples were then centrifuged at 900 g for 10 min at 4°C , and resulting nuclei pellet was resuspended in blocking buffer in preparation for immunolabel-based sorting.

Fluorescence-activated cell sorting for astrocytic nuclei enrichment

All procedures were completed on ice or at 4°C, and centrifugations were completed at 400 g for 5 min at 4°C unless otherwise specified. Post-isolation, nuclei suspensions were incubated in blocking buffer (0.8% reagent-grade bovine serum albumin (BSA; Prolian BioLogicals, 68700), 0.5% Rnasin Plus, and 10% goat serum (MP Biomedicals, 191356) in 1× phosphate buffer saline (PBS; VWR, 16750–102)) for 20 min. Each sample was split into aliquots in order to prepare all respective controls for sorting, including unstained, secondary antibody-only, and single antibody-labeled controls. All antibody dilutions were prepared in fluorescence-activated cell sorting (FACS) buffer (0.8% reagent-grade BSA and 0.5% Rnasin Plus in 1× PBS). Samples were then pelleted, resuspended in either FACS buffer or diluted primary antibodies, and incubated on ice for 20 min in the dark. Post-incubation, samples were pelleted and washed with FACS buffer prior to resuspension in FACS buffer or diluted secondary antibodies. Finally, samples were pelleted and washed with FACS buffer prior to resuspension in FACS buffer for sorting. Immediately prior to sorting, samples were spiked with '4',6 diamidino 2 phenylindole, dihydrochloride (DAPI; Thermo Fisher Scientific, D1306, 1:10,000) in order to better visualize nuclei. All samples were sorted using a MoFlo XDP sorter with a 100-μm nozzle at 4°C. Unstained, isotype control, and single antibody-labeled controls were used to establish gating scheme for each donor (see [Figure S2](#) for representative gating schemes). All sorting data was visualized and quantified using FlowJo (v10.7.1).

SOX9 sorts

Primary antibodies used for SOX9-based sorts included: anti-SOX9 (Abcam, Cambridge, ab185966, 1:100) and rabbit IgG isotype control (Abcam, ab172730, 1:200). Primary antibodies were detected with goat anti-rabbit IgG (H&L) secondary antibody conjugated to Alexa Fluor 594 (Thermo Fisher Scientific, R37117, 2 drops/mL). Gates were set to collect DAPI⁺ and SOX9⁺ singlet events, and on average, ~75,000 DAPI⁺/SOX9⁺ nuclei were captured per pilot donor (see [Table S3](#) for all SOX9 sorting outputs).

LHX2⁺/NeuN⁻ sorts

Primary antibodies used for LHX2⁺/NeuN⁻-based sorts included: anti-LIM Homeobox 2 LHX2 (EMD Millipore, AB5756, 1:500), anti-NeuN (Millipore Sigma, MAB377, 1:2500), rabbit IgG isotype control (Abcam, ab172730, 1:1000), mouse IgG1 isotype control (Millipore Sigma, MABC002, 1:1250). Primary antibodies were detected with goat anti-rabbit IgG (H&L) secondary antibody conjugated to Alexa Fluor 488 (Invitrogen, A11034, 1:4,000) or goat anti-mouse IgG (H&L) secondary antibody conjugated to Alexa Fluor 647 (Invitrogen, A21235, 1:7,000), respectively. Gates were set to collect DAPI⁺, LHX2⁺, and NeuN⁻ singlet events, and on average, ~88,000 DAPI⁺/LHX2⁺/NeuN⁻ nuclei were captured per donor (see [Table S3](#) for all LHX2⁺/NeuN⁻ sorting outputs).

snRNA-seq pipeline

After sorting, collected nuclei were pelleted at 900 g for 10 min at 4°C, were resuspended in ~50 μL of 0.04% BSA in PBS, and counted using a hemocytometer. Based on nuclei counts, samples were then resuspended in additional 0.04% BSA in PBS buffer in order that nuclei concentrations were ideal for 10× chromium loading (between 100 and 1,700 nuclei/μL). Nuclei were processed using the Single Cell 3' Gene Expression kit v3 (10× chromium, 1000076) according to manufacturer's instructions. In brief, 4,800–16,000 nuclei per sample were loaded onto Single Cell Chips B in order to recover as many nuclei as possible (targeting 3,000–10,000 nuclei per sample), while limiting potential for doublets. Using a Chromium Controller, Gel Bead-In Emulsions were generated, and samples were subsequently processed to isolate and amplify cDNA and ultimately construct libraries. Quality and concentration of cDNA was evaluated on an Agilent 2100 Bioanalyzer. Quality and concentration of libraries were evaluated by qPCR and on an Agilent 2200 TapeStation, and libraries were sequenced on Illumina NovaSeq 6000 through NYU Langone's Genomic Technology Core. Basecalling was completed using Illumina NovaSeq 6000 RTA v3.4.4 software, and BCL base call files were converted to FASTQ files using bcl2fastq Conversion software (v2.20). Using Cell Ranger software suite (v4.0.0) (10X Genomics), FASTQ files were aligned to a pre-mRNA-modified GRCh38 human reference genome (modification steps provided by 10X Genomics), and gene-bar code count matrices were generated for all demultiplexed samples.

snRNA-seq data analysis

The majority of code used to evaluate snRNA-seq data is based off of analysis completed in the original *Muscat* R package vignette ([Crowell et al., 2019](#)). This process was repeated separately for the SOX9-sorted pilot donor cohort as well as for iterations of LHX2⁺/NeuN⁻-sorted donor cohort. Exact code used to analyze each dataset analysis is provided on the Liddelow Lab GitHub page: https://github.com/liddelowlab/Sadick_et_al_2022.

Quality control

All sample raw gene-bar code count matrices were converted into a *SingleCellExperiment* (SCE) object in R (v3.6.1–4.0.3) for initial quality control filtering ([Amezquita et al., 2020](#)). Undetected genes were removed based on the total summed counts per gene. Doublets were removed using *scds*, in which a threshold was applied assuming that 1% of every 1,000 nuclei captured was a doublet. Sample-specific outliers were identified using *scater::isOutlier*, and nuclei were removed if total counts, total features, and/or percentage of mitochondrial genes was greater than 2.5 median absolute deviations away from the sample median. Finally, genes were only kept if they had a count of at least one in more than 20 nuclei. After filtering SOX9-sorted donor pilot data, a total of 18,991 nuclei remained across 2 NS and 3 AD patients, with a median of 8,885 counts and 3,406 features per nucleus. After filtering LHX2⁺/NeuN⁻-sorted donor data (final donor cohort), a total of 80,247 nuclei remained across 5 NS and 9 AD patients, with a median of 6,714 counts and 2,929 features per nucleus.

Normalization, integration, and dimension reduction

Functions in the *Seurat* (v3.2.2) package were used for the following analyses (Stuart et al., 2019). Data were log normalized, and the top 2,000 variable features were identified on a per sample basis. Samples were then anchored and integrated using Canonical Correlation Analysis (dims = 30). After scaling the data, linear and non-linear dimension reduction was performed by Principle Component Analysis of variable features and t-Distributed Stochastic Neighbor Embedding (tSNE) analysis, respectively, using the top 30 principle components. For each dataset, the number of dimensions used for dimensional reduction analyses was determined based on the inflection point on an Elbow plot.

Clustering, annotation, and marker identification

Clustering was calculated using the functions *FindNeighbors* and *FindClusters*, with a range in resolution between 0.1 and 1. Ultimately, for each dataset, a resolution of 0.1 was used for initial clustering. To identify major cell types present, the *FindAllMarkers* function (\log_2 fold change > 0.25, using Wilcoxon rank sum test, adjusted p-value < 0.05 using the Bonferroni correction) was used to determine unique and/or highly enriched DEGs in one cluster compared to all other clusters. These cluster-specific features were then queried against a set of canonical cell type-specific markers from the literature. Data were visualized using *Seurat* package functions, including DimPlot, FeaturePlot, DotPlot, VlnPlot, and DoHeatmap. For SOX9-positive sorted data, only 6.6% of nuclei were astrocytes, while the vast majority of nuclei (72.2%) were neurons. For LHX2⁺/NeuN⁻-based sorted data, astrocytes made up the largest captured nuclei population (51.5%), with the second largest captured nuclei population as oligodendrocytes (29.7%). Please refer to Table S3 for cell type captures and DEGs identified for each sorting strategy.

Cell type-specific sub-clustering

Using the function *Seurat::subset*, astrocyte and oligodendrocyte nuclei were reanalyzed in isolation. For SOX9-based sorts, 1,832 astrocytes were analyzed. For LHX2⁺/NeuN⁻-based sorts (final cohort), 41,340 astrocytes and 23,840 oligodendrocytes were analyzed, respectively. Astrocyte- and oligodendrocyte-specific analyses were completed as described above (from identifying a new set of top 2,000 variable features through clustering and marker identification). Please note that two rounds of subsetting and analysis were required for LHX2⁺/NeuN⁻-sorted astrocytes in order to remove contaminating, non-astrocytic nuclei. Please see to Table S3 for the number of principle components and resolutions used in each analysis as well as astrocyte- and oligodendrocyte-specific DEGs. Data were visualized using *Seurat* package functions (as listed above). Additionally, DEGs for LHX2⁺/NeuN⁻-sorted astrocytes and oligodendrocytes were evaluated by pathway analysis. In brief, cluster-specific astrocyte or oligodendrocyte DEG gene IDs were converted to Ensembl IDs (using *AnnotationDbi* package *org.Hs.eg.db::mapIDs*) and then to Entrez IDs (using *biomaRt::getBM*). For each individual cluster in each cell type, Entrez IDs were analyzed using *clusterProfiler::enrichGO*, and GO terms were identified (adjusted p-values < 0.05 using the Benjamini-Hochberg method, false discovery rate < 0.1) (Table S3).

Cluster-specific differential gene expression and pathway analysis

Differential gene expression and pathway analysis was completed for LHX2⁺/NeuN⁻-sorted astrocyte and oligodendrocyte clusters in parallel. For each cluster in each cell type, these analyses were completed based on disease state (i.e., comparing all NS donors with AD donors). Data was read in using the *Seurat::subset* function. The subsetted *Seurat* object was then converted into a SCE object for additional threshold filtering. Lowly expressed genes were removed, as identified by having fewer than 5 transcripts counted in less than 5 cells. Then, the top 2000 variable genes were identified using *scran::modelGeneVar* and *getTopHVG* functions, and the *zinbwave* function was run using observational weights generated for each gene (K = 0, epsilon = 1e12) (Risso et al., 2018). The remaining DEG analysis was completed using the *edgeR* package (Robinson et al., 2010) by calculating normalized factors, estimating dispersion, model fitting using *glmFit*, comparing disease state (i.e., NS versus AD), and passing *zinbwave*-generated observational weights to the *glmWeightedF* function. Genes were identified as DEGs if they had an adjusted p-value < 0.05 using the Benjamini-Hochberg method and had a \log_2 fold change > ±0.25. For pathway analysis, all DEGs were converted to their Ensembl IDs and subsequently their Entrez IDs (as described above) prior to being separated into upregulated and downregulated lists with their accompanying \log_2 fold changes. Each list was then analyzed separately to determine upregulated and downregulated GO terms (as described above). DEGs were visualized using *ComplexHeatmap::heatmap* function. Upregulated and downregulated DEGs as well as GO terms were compared across clusters and were visualized using *UpSetR* package. Lists of DEGs and pathways are provided in Tables S4 and S5.

Reanalysis of previously published snRNA-seq and scRNA-seq datasets

We obtained FASTQ files from previously published snRNA-seq (Grubman et al., 2019; Mathys et al., 2019; Zhou et al., 2020) datasets in order that all datasets were analyzed under identical protocols to our own generated data, as described above beginning at alignment using the Cell Ranger software suite (v4.0.0). All snRNA-seq datasets were aligned to the pre-mRNA-modified GRCh38 human reference genome. As described above, each dataset was processed for quality control, normalization, anchoring, integration, dimension reduction, clustering, annotation, and marker identification (Figure S6). For each dataset, astrocyte and oligodendrocyte nuclei were subsetted as unique *Seurat* objects for reanalysis in isolation (Figures 3 and 7). For Mathys astrocyte and oligodendrocyte subsetted analyses, multiple donors were removed because their nuclei yields were lower than the number of principle components used to evaluate the data (donors removed are listed in Table S1). Please note that reference-based integration was used for all objects in Mathys and Zhou datasets due to memory constraints (parameters listed in Table S1). Additionally, please note that two rounds of subsetting and analysis were required for Zhou astrocytes in order to remove contaminating, non-astrocytic nuclei/cells.

Principle components/resolution used for analyses, cell type captures, and DEGs identified per cluster per dataset are listed in [Table S1](#).

Cell type-specific multi-dataset analyses

Once only astrocyte and oligodendrocyte *Seurat* objects were created for each dataset, we merged either all astrocyte- or oligodendrocyte-specific objects to create two multi-dataset objects: (1) astrocyte nuclei from Mathys, Grubman, Zhou, and our LHX2⁺/NeuN⁻-sorted snRNA-seq datasets ([Figure 7](#)) and (2) oligodendrocyte nuclei from Mathys, Grubman, Zhou, and our LHX2⁺/NeuN⁻-sorted snRNA-seq datasets ([Figure 3](#)). Once individual dataset cell type-specific *Seurat* objects were merged using the function *Seurat::merge*, multi-dataset objects were processed as described above (from identifying a new set of top 2,000 variable features through clustering and marker identification). Reference-based integration was used for astrocyte and oligodendrocyte nuclei snRNA-seq merged objects due to memory constraints (parameters listed in [Table S5](#)). Please refer to [Table S5](#) for multi-dataset cell type-specific cluster yields and DEGs identified.

Analysis of previously published spatial transcriptomic data

Code used to analyze the spatial localization of astrocyte gene signatures is available on the Liddelow Lab GitHub page: https://github.com/liddelowlab/Sadick_et_al_2022. All statistics, plots, and analysis for this portion of the manuscript were created with R (v4.1.1). Figure S12A and species icons in Figures 6 and S12 were created with BioRender.com.

Datasets

Previously published 10X Visium spatial transcriptomics data from twelve pathology-free human dorsolateral prefrontal cortex (DLPFC) samples (3 donors)([Maynard et al., 2021](#)) was obtained from the Globus repository (available at http://research.libd.org/globus/jhpce_HumanPilot10x/index.html) in the form of filtered feature-barcode matrices, corresponding TIFF images, and spot coordinate TSV files. We also used our lab's recently published 10X Visium data from whole hemisphere saline or LPS-injected mice (n = 3 per condition), referred to in this manuscript as "healthy"/"control" and "inflamed" (data available at the Gene Expression Omnibus repository: series GSE165098)([Hasel et al., 2021](#)). These mice were injected intraperitoneally with saline or 5 mg/kg lipopolysaccharide (LPS), and tissue was collected 24 h post-injection.

Creating astrocyte cluster gene modules

We defined gene signatures for each astrocyte cluster using positive marker genes (\log_2 fold change > 0.3, adjusted p-value < 0.05) from our earlier differential expression testing (see [Cluster-specific differential gene expression and pathway analysis](#) and [Table S3](#)). To explore expression of these gene signatures in the mouse data as well, we created mouse gene modules comprised of one-to-one orthologs of the human module genes, which we identified using the *biomaRt* R package (v2.48.3) ([Durinck et al., 2009](#)). These mouse gene modules were then filtered to remove genes not expressed in the spatial transcriptomics data. The resultant modules of genes for each astrocyte cluster are available in [Table S7](#). We also created mouse modules using these same methods for genes upregulated in each astrocyte cluster in AD (\log_2 fold change > 0.5, adjusted p-value < 0.05) using our differential expression testing results (see [Cluster-specific differential gene expression and pathway analysis](#) and [Table S6](#)). The genes comprising these AD gene modules are also available in [Table S7](#).

Regional annotation

Human: the spots in the human spatial transcriptomics dataset were previously manually annotated with their cortical layer locations by Maynard et al., and these annotations were retrieved using the *spatialLIBD* R package (v1.4.0) ([Pardo et al., 2021](#)). Layers 2 and 3 were combined and labeled layer 2/3 to aide in comparison to the mouse dataset. Mouse: to first identify spots as WM or gray matter, we assigned WM scores to individual spots on the basis of expression of WM/myelin genes (*Mbp*, *Mobp*, *Plp1*, *Mag*, *Mog*, and *Mal*) using the *AddModuleScore* function in *Seurat* (v4.0.5) ([Hao et al., 2021](#)) ([Figure S12C](#), see *Differential Enrichment Testing* for detailed explanation of module score calculations). Initial classification of spots as WM or gray matter was then determined by thresholding the WM module score; spots with a module score greater than the 78.75th percentile were classified as WM, and spots below this threshold were classified as gray matter. This threshold was chosen based on agreement with anatomy apparent from the H&E staining. Individual spot classification was then manually adjusted to correct mistaken assignments (e.g., a spot clearly in the corpus callosum but assigned as gray matter). Gray matter spots were then labeled with their cortical layer location based on gene expression. To this end, spot-level gene expression data was log-normalized. Then top 3,000 highly variable genes most common across the six samples were identified using the *FindIntegrationFeatures* function. Technical variables (the number of genes detected per spot, the number of UMIs per spot, and the percentage of UMIs mapping to the mitochondrial genome per spot) were regressed against each gene in the normalized feature-barcode matrix, and the residuals were scaled and centered. PCA was then performed on the scaled data, using the previously identified highly variable genes. The resulting PCA embeddings were then iteratively corrected to remove the effects of sample identity and condition (LPS or saline) using the *Harmony* R package (v0.1.0) ([Korsunsky et al., 2019](#)). UMAP dimensionality reduction was then performed using the first 15 principal components from the integrated, corrected PCA embeddings. A shared nearest-neighbor graph was constructed using the *FindNeighbors* function, and unbiased Louvain clustering was performed using the *FindClusters* function with a resolution parameter of 0.6. Several resolution parameters were examined, and 0.6 was selected because the resultant clusters appeared to map most closely to the layers of the cortex. Four clusters appearing largely in the retrosplenial and somatomotor areas were subsetted, re-integrated, and sub-clustered using identical methods to capture the cortical layers in those regions (with 2,000 variable features, 20 principal components for UMAP dimensionality reduction and

clustering, and a clustering resolution parameter of 0.5). In aggregate, clustering and sub-clustering the cortical mouse Visium spots resulted in 11 clusters, which were each largely contained within one cortical layer. Each cluster was then assigned to a cortical layer—L1, L2/3, L4, L5, or L6—based on its position in the Visium sections and its average expression of canonical markers. Finally, the individual layer labels were adjusted for individual outlier spots to match their true anatomical locations. Final cortical layer groups were generally well separated on the basis of gene expression (Figure S12D), validating their annotations. To verify that our mouse cortical layers were well labeled and comparable to the previously annotated human Visium data, we next sought to compare the cross-species similarity of each cortical layer. To this end, we z-scored the average expression of all one-to-one orthologous genes that were highly variable (top 3,000 genes) in both the human and mouse Visium datasets across the cortical layers in each dataset (in total, 707 genes). We then calculated the Spearman correlation coefficients for all layer combinations between the datasets. This revealed each cortical layer in a given species was most highly correlated with the same cortical layer in the corresponding species (Figure S12E), supporting the validity of our mouse cortical layer annotations and cross-species comparison of the spatial transcriptomics datasets.

Differential enrichment testing

To quantify enrichment of astrocyte subtype and reactive sub-state gene signatures across cortical regions, we first calculated expression scores for each gene module within each spatial transcriptomics spot using *Seurat* and the *AddModuleScore* function (Hasel et al., 2021; Tirosh et al., 2016). In summary, module scores reflect the average expression of the gene set subtracted by expression of a control gene set 100 times larger than the gene module, where each gene in the module is matched with 100 genes in the control gene set with similar expression levels (Tirosh et al., 2016). Subtraction of the control gene set allows for standardization of module scores across spots and Visium sections despite technical variation. Most astrocyte cluster gene modules contained dozens or even hundreds of genes, making these module scores robust to gene drop out and technical variation. To test whether each cluster gene module differed in enrichment across cortical regions, we pooled all sections of a given species together and compared gene module scores between spots of each cortical region (L1–L6 and WM) using a Kruskal-Wallis test with a Bonferroni correction for multiple comparisons. All cluster gene modules exhibited statistically significant differences (adjusted p-value < 0.05; see Table S7 for test statistics and p-values). To compare how strongly different cluster modules varied in score across the cortex in Figure S12F, Kruskal-Wallis H test statistics were z-scored within each species and a heatmap was created using the *ComplexHeatmap* R package (v2.8.0) (Gu et al., 2016). To test whether each gene module was enriched (more highly expressed) or de-enriched (less highly expressed) in a given cortical region compared to the rest of the cortex, we next performed Wilcoxon rank sum tests with Bonferroni multiple comparisons corrections comparing the spots from a given region to all other spots (pooling all other cortical regions; see Table S7 for p-values and test statistics). For Figures 6A and 6B; Figure S12G, + or – symbol indicates the gene module is significantly enriched or de-enriched, respectively, in a given cortical region compared to the rest of the cortex (adjusted p-value < 0.05). The sign of the symbol corresponds to the sign (positive or negative) of the median of the estimated difference between a spot from the cortex region in question compared to spots from the rest of the cortex (i.e., the median location shift). We next tested whether cluster gene modules were upregulated between spots from the inflamed (LPS-injected) mouse brain compared to the control (saline-injected) brain using Wilcoxon rank sum tests with Bonferroni corrections (Table S7). Lastly, we examined whether AD gene modules for each astrocyte subtype were upregulated in spots from the inflamed mouse brain compared to controls using Wilcoxon rank sum tests with Bonferroni corrections (Table S7). For Figures 6E and 6F; Figure S12H, + or – symbols indicate the gene module is significantly enriched or de-enriched, respectively, in spatial transcriptomics spots from the LPS-injected samples compared to spots from the saline-injected samples within the indicated cortical region (adjusted p-value < 0.05). For all box and density plots in Figure 6; Figure S12: transecting line denotes the median; notches denote the 95% confidence interval surrounding the median; and whiskers denote 1.5× the interquartile range. All box and density plots were created with the *ggplot2* (v3.3.5) and *ggridist* (v3.0.1) (Kay, 2021) packages in R.

Visualization

Visualization of astrocyte cluster gene signatures across representative Visium sections is challenging given sparse expression, the prevalence of gene drop out in spatial transcriptomics data, and the size of Visium spots (which often capture several cells within each spot). To overcome these difficulties, we utilized a recent Bayesian method of spatial gene expression resolution enhancement (Zhao et al., 2021). Individual samples were first normalized with *Seurat* (Hafemeister and Satija, 2019), then preprocessing, PCA, and spatial clustering were performed using the *BayesSpace* R package (v1.2.1) (Zhao et al., 2021). For the human samples, seven clusters (chosen based on the elbow in a log-likelihood plot) and 15 principal components (chosen based on the elbow in a plot of the standard deviation of each principal component from the PCA results) were used for spatial clustering. For the mouse samples, 20 principal components and 17–18 clusters were used. Spatial clustering was then enhanced to sub-spot resolution using the *spatialEnhance* function with default parameters. Spatial gene expression for all genes was then enhanced to sub-spot resolution using the *enhanceFeatures* function, which fits a linear model for each gene with the top principal components from each spot and predicts sub-spot expression using this model. We then calculated enrichment scores for each sub-spot using the above module score method (see *Differential Enrichment Testing*) with the same gene modules (see *Creating astrocyte cluster gene modules*) using the resolution-enhanced expression data. Enrichment scores were then plotted with a minimum-maximum scale on representative sections. We found calculating enrichment scores using these resolution enhancement methods aided in recognition of spatial patterns and were generally representative of spot-level module score patterns within each cortical region (Figure S12B). All differential enrichment testing and statistical tests were performed using original, spot-level gene expression

and module scores; Bayesian resolution-enhanced gene expression and enrichment scores were only used for visualization.

QUANTIFICATION AND STATISTICAL ANALYSIS

Statistics

Throughout this manuscript, quantified cell/nuclei outputs are displayed as the arithmetic mean (\pm s.d., if applicable), and plots were generated using the *ggplot2* and *ggpubr* packages in R and/or using GraphPad Prism (v9.0.0) unless otherwise noted. Please note that all quantified raw values for sorting yields, IHC measurements, snRNA-seq and spatial transcriptomics analyses are also available in Tables S1–S7.

Wilcoxon test

For Figure 1A, statistical tests used were two-tailed Wilcoxon signed-rank tests ($\alpha = 0.05$). All quantification and analysis were performed blinded to the condition of the donors.

Randomization

No randomization was used in the analysis of snRNA-seq or IHC imaging data.

Sample size estimation

No methods were used to predetermine the sample size used in this study. However, our donor cohort is similar in size to published works (Grubman et al., 2019; Leng et al., 2021).

ADDITIONAL RESOURCES

The following datasets were produced during this study and are available for download and further analysis.

Cell Image Library: <http://cellimagelibrary.org/groups/54423>

All pathology imaging data are available through the Cell Image Library repository.

Raw sequencing data

<https://www.ncbi.nlm.nih.gov/geo/query/acc.cgi?acc=GSE167494>

Raw single nuclei RNA sequencing (snRNA-seq) data generated in this study (including both FASTQ and Cell Ranger-generated matrix files) are available at GEO (Gene Expression Omnibus) under accession number GSE167494.

Analyzed snRNA-seq data (pseudobulk): www.gliaseq.com

We created an open-access, interactive website as a resource to share and easily navigate our analyzed snRNA-seq data for astrocytes and oligodendrocytes.

GitHub

https://github.com/liddelowlab/Sadick_et_al_2022

All code for analysis of original and previously published snRNA-seq and spatial transcriptomic datasets are available on the Liddelow Lab GitHub page.